

University of Groningen

Constraining the mass density of free-floating black holes using razor-thin lensing arcs

Banik, Uddipan; van den Bosch, Frank C.; Tremmel, Michael; More, Anupreeta; Despali, Giulia; More, Surhud; Vegetti, Simona; McKean, John P.

Published in:
Monthly Notices of the Royal Astronomical Society

DOI:
[10.1093/mnras/sty3267](https://doi.org/10.1093/mnras/sty3267)

IMPORTANT NOTE: You are advised to consult the publisher's version (publisher's PDF) if you wish to cite from it. Please check the document version below.

Document Version
Publisher's PDF, also known as Version of record

Publication date:
2019

[Link to publication in University of Groningen/UMCG research database](#)

Citation for published version (APA):

Banik, U., van den Bosch, F. C., Tremmel, M., More, A., Despali, G., More, S., Vegetti, S., & McKean, J. P. (2019). Constraining the mass density of free-floating black holes using razor-thin lensing arcs. *Monthly Notices of the Royal Astronomical Society*, 483(2), 1558-1573. <https://doi.org/10.1093/mnras/sty3267>

Copyright

Other than for strictly personal use, it is not permitted to download or to forward/distribute the text or part of it without the consent of the author(s) and/or copyright holder(s), unless the work is under an open content license (like Creative Commons).

The publication may also be distributed here under the terms of Article 25fa of the Dutch Copyright Act, indicated by the "Taverne" license. More information can be found on the University of Groningen website: <https://www.rug.nl/library/open-access/self-archiving-pure/taverne-amendment>.

Take-down policy

If you believe that this document breaches copyright please contact us providing details, and we will remove access to the work immediately and investigate your claim.

Downloaded from the University of Groningen/UMCG research database (Pure): <http://www.rug.nl/research/portal>. For technical reasons the number of authors shown on this cover page is limited to 10 maximum.

Constraining the mass density of free-floating black holes using razor-thin lensing arcs

Uddipan Banik,¹★ Frank C. van den Bosch¹, Michael Tremmel,^{2,3}
Anupreeta More^{4,5}, Giulia Despali⁶, Surhud More,^{4,5} Simona Vegetti⁶ and John
P. McKean^{7,8}

¹*Department of Astronomy, Yale University, PO Box 208101, New Haven, CT 06520, USA*

²*Department of Physics, Yale University, PO Box 201820, New Haven, CT 06520, USA*

³*Yale Center for Astronomy and Astrophysics, PO Box 208121, New Haven, CT 06520, USA*

⁴*Kavli Institute for the Physics and Mathematics of the Universe (WPI), Todai Institutes of Advanced Study, University of Tokyo, 5-1-5 Kashiwanoha, Kashiwa 277-8583, Japan*

⁵*The Inter-University Center for Astronomy and Astrophysics, Post Bag 4, Ganeshkhind, Pune 411007, India*

⁶*Max Planck Institute for Astrophysics, Karl-Schwarzschild-Strasse 1, D-85740 Garching, Germany*

⁷*ASTRON, Netherlands Institute for Radio Astronomy, Postbus 2, NL-7990 AA Dwingeloo, the Netherlands*

⁸*Kapteyn Astronomical Institute, PO Box 800, NL-9700 AV Groningen, the Netherlands*

Accepted 2018 November 26. Received 2018 November 16; in original form 2018 September 6

ABSTRACT

Strong lensing of active galactic nuclei in the radio can result in razor-thin arcs, with a thickness of less than a milliarcsecond, if observed at the resolution achievable with very long baseline interferometry (VLBI). Such razor-thin arcs provide a unique window on the coarseness of the matter distribution between source and observer. In this paper, we investigate to what extent such razor-thin arcs can constrain the number density and mass function of ‘free-floating’ black holes, defined as black holes that do not, or no longer, reside at the centre of a galaxy. These can be either primordial in origin or arise as by-products of the evolution of supermassive black holes in galactic nuclei. When sufficiently close to the line of sight, free-floating black holes cause kink-like distortions in the arcs, which are detectable by eye in the VLBI images as long as the black hole mass exceeds ~ 1000 Solar masses. Using a crude estimate for the detectability of such distortions, we analytically compute constraints on the matter density of free-floating black holes resulting from null-detections of distortions along a realistic, fiducial arc, and find them to be comparable to those from quasar milli-lensing. We also use predictions from a large hydrodynamical simulation for the demographics of free-floating black holes that are not primordial in origin and show that their predicted mass density is roughly four orders of magnitude below the constraints achievable with a single razor-thin arc.

Key words: gravitational lensing: strong – techniques: high angular resolution – quasars: supermassive black holes – dark matter.

1 INTRODUCTION

Strong gravitational lensing is a powerful tool to probe the distribution of matter in our Universe on a variety of scales and across a large range in redshift (e.g. Schneider, Ehlers & Falco 1992; Treu 2010). Particularly powerful is the notion that strong gravitational lensing can be used to probe the coarseness of the matter distribution along the line of sight by looking for *distortions* of arcs, arclets, rings, or multiply imaged sources arising from the strong gravita-

tional lensing of some source due to a much more massive object. These distortions come in the form of flux-ratio anomalies (e.g. Mao & Schneider 1998; Dalal & Kochanek 2002; Mao et al. 2004; Metcalf 2005), modified time-delays (also known as the Shapiro delay, Keeton & Moustakas 2009; Mohammed, Saha & Liesenborgs 2015), or distortions in extended arcs (e.g. Koopmans 2005; More et al. 2009; Vegetti & Koopmans 2009; Vegetti et al. 2010, 2012; Hezaveh et al. 2016b; Birrer, Amara & Refregier 2017).

A particularly exciting development has been the use of image distortions to probe the abundance of dark matter (sub)haloes on subgalactic scales, which holds the potential to shed light on the nature of dark matter (e.g. Li et al. 2016, 2017; Hezaveh et al.

* E-mail: uddipan.banik@yale.edu

2016a; Bayer et al. 2018; Despali et al. 2018; Vegetti et al. 2018). In general, detecting lower mass haloes requires higher sensitivity, which in turn implies higher spatial resolution, or more small-scale structure in the source. Hence, one ideally wants to use arcs and Einstein rings that have been observed at the highest possible resolution. Over the last few years, state-of-the-art observations at radio and submillimetre wavelengths, with very long baseline interferometry (VLBI) and with the long baselines of the Atacama Large (sub)Millimetre Array (ALMA), respectively, have revealed a number of extremely thin lensing arcs, with a thickness of around 2–25 mas (e.g. ALMA Partnership et al. 2015; Wong et al. 2017; Spingola et al. 2018). These are ideally suited to probe the presence of low-mass perturbers ($10^5 M_\odot \lesssim M \lesssim 10^8 M_\odot$) along the line of sight between the source and the observer, and of low-mass substructure associated with the main lens.

These perturbers may consist of a wide variety of objects, including dark matter (sub)haloes, dwarf galaxies, globular clusters, and black holes. Among these, dark matter (sub)haloes are of particular interest, as being able to constrain their number density over the mass range $10^5 M_\odot \lesssim M \lesssim 10^8 M_\odot$ holds the potential to constrain the nature of dark matter (in particular, the mass of a Weakly Interacting Massive Particle). However, dark matter (sub)haloes are also relatively diffuse objects, and unless they are relatively massive ($M \gtrsim 10^9 M_\odot$) their impact on the razor-thin arcs is only detectable through sophisticated image analysis¹ such as in the studies by Vegetti et al. (2010, 2012, 2014), Hezaveh et al. (2016b), and Birrer et al. (2017). In this paper, we therefore focus on another type of perturber, namely black holes. Due to their extreme compactness, they cause a maximal, and therefore most easily detectable, distortion for a given mass. Throughout we focus on free-floating black holes, which we define as black holes that are well-separated from the stellar bodies of galaxies, and we investigate the relation between the number density of such free-floating black holes and the probability of detecting one or more distortions along razor-thin gravitational lensing arcs. In particular, we restrict ourselves to distortions that are easily detectable ‘by eye’ in the images inferred from the VLBI data without sophisticated analysis. As we demonstrate below, such distortions are kink-like in shape.

There are different mechanisms that can give rise to free-floating black holes. On the one hand, they can be ‘primordial’ in origin and be generated by one of three mechanisms: through some form of cosmological phase transition (e.g. Hawking, Moss & Stewart 1982; Kodama, Sasaki & Sato 1982), through a temporary softening of the equation of state (e.g. Jedamzik 1997), or through the collapse of large inhomogeneities (Carr & Lidsey 1993; Leach, Grivell & Liddle 2000). Such primordial black holes (PBHs) are an intriguing candidate for the dark matter. However, very stringent constraints have been obtained on the mass density of PBHs from a wide variety of studies (see Carr, Kühnel & Sandstad 2016 for a comprehensive review), leaving little room for PBHs making up all of the dark matter, especially if the PBHs are massive ($M_{\text{BH}} \gtrsim 10^3 M_\odot$). Nevertheless, even if such massive PBHs only provide a small fraction of the dark matter, they may have important consequences; in particular, they could act as seeds for the supermassive black holes (SMBHs) in galactic nuclei (e.g. Carr & Silk 2018). At masses above $\sim 10^3 M_\odot$, the dominant constraint on the number density of PBHs comes from the cosmic microwave background (CMB). Massive PBHs will accrete matter prior to recombination, and the resulting radiation output would leave imprints on the spectrum and

anisotropies of the CMB that have not been observed (e.g. Ricotti, Ostriker & Mack 2008), ruling out that PBHs with masses in the range $10^3 M_\odot \lesssim M_{\text{BH}} \lesssim 10^{11} M_\odot$ contribute more than a fraction 10^{-5} of the dark matter (but see Ali-Haïmoud & Kamionkowski 2017 for more conservative constraints). Inoue & Kusenko (2017) have also obtained upper bounds on the PBH abundance from the observation of X-ray compact objects in galaxies in the mass range of $1 M_\odot \lesssim M_{\text{BH}} \lesssim 2 \times 10^7 M_\odot$.

However, there is an alternative formation mechanism for free-floating BHs in the mass range $10^3 M_\odot \lesssim M_{\text{BH}} \lesssim 10^{11} M_\odot$ as mentioned above, which operates well after recombination, thereby evading the CMB constraints. This mechanism is a by-product of the galaxy formation and evolution process. It is well known that galaxies harbour SMBHs in their centres with a mass that is tightly correlated with the velocity dispersion of the stellar body (Tremaine et al. 2002). Due to the hierarchical nature of structure formation, galaxies merge, during which the SMBHs of the progenitors sink to the centre of the merger remnant, where they form a SMBH binary. If a new merger occurs before the binary has coalesced, this merger scenario may give rise to SMBH triplets (e.g. Deane et al. 2014). The three-body interaction of such a triplet can result in the ejection of one of the SMBHs, which can thus become unbound and free-floating. In addition, the coalescence of a binary SMBH can result in a velocity kick, which can be sufficiently large as to unbind the resulting SMBH remnant from a low-mass galaxy (Favata, Hughes & Holz 2004; González et al. 2007). Finally, the tidal forces acting on satellite galaxies as they orbit their host halo may strip them apart, resulting in free-floating black holes orbiting the central galaxy. If the orbit is sufficiently far from the galactic centre, or the halo has a substantially dense core, dynamical friction from the host halo can be sufficiently small that such free-floating BHs survive for longer than the Hubble time (e.g. Di Cintio et al. 2017; Tremmel et al. 2018a,b). In what follows we shall refer to these free-floating black holes that form as a by-product of galaxy formation as ‘wandering’ black holes, in order to distinguish them from the PBHs discussed above.

The existence of wandering SMBHs far from the galactic centre has been predicted using both cosmological simulations (Bellovary et al. 2010; Volonteri et al. 2016) and semi-analytic models (Volonteri & Perna 2005). Only recently have large-scale cosmological simulations been able to accurately follow the dynamics of SMBHs within galaxies down to sub-kpc scales (Tremmel et al. 2015, 2017). In particular, Tremmel et al. (2018b) use data from the ROMULUS25 cosmological simulation to predict that wandering SMBHs should be common-place in Milky Way-mass haloes at $z = 0$, with ~ 10 existing within the virial radius.

As is evident from the discussion above, constraining the number density and mass function of free-floating black holes can put powerful constraints on both inflationary models and the various physical mechanisms at play during the formation and evolution of SMBHs. Free-floating BHs are located in regions with little gas and/or stars, and they are therefore unlikely to reveal their presence through the emission associated with the accretion of matter. However, they can reveal their presence through the gravitational distortion of (razor-thin) lensing arcs, which is the phenomenon we investigate in this paper. Interestingly, as this paper was close to completion, Chen et al. (2018) reported a possible detection of an SMBH of mass $8.4^{+4.3}_{-1.8} \times 10^9 M_\odot$ offset by 4.4 ± 0.3 kpc from the centre of the main lensing galaxy, the brightest cluster galaxy of MACS J1149 + 2223.5 at $z = 0.54$. The presence of a SMBH is inferred through a kink-like distortion in one of the multiply-lensed images of the background source. Although other explana-

¹In the case of interferometric data, this is best done in the UV plane.

tions for the observed structure are possible, such a detection would be a wonderful proof of concept for the methodology advocated here.

This paper is organized as follows. In Section 2, we discuss the double lens configuration comprising a dark matter halo as the main lens plus a black hole along the line of sight, which acts as a secondary lens or a perturber distorting the arc produced by the main lens. In Section 3, we discuss the criteria under which the presence of such a black hole is detectable as a perturbation of the lensing arc, which we use in Section 4 to compute constraints on the comoving number density of black holes, given some detection, or lack thereof. Section 5 discusses the kind of constraints that are realistically achievable, and we summarize our findings in Section 6. We also provide an Appendix in which we compare the lensing distortion effect of BHs to that of subhaloes as well as derive a number of useful scaling relations showing the dependence of the constraints on the mass density of free-floating black holes on the black hole mass and the spatial resolution of the data.

Throughout this paper, we adopt the Planck 2014 cosmology (Planck Collaboration XVI 2014) with $H_0 = 67.8 \text{ km s}^{-1} \text{ Mpc}^{-1}$, $\Omega_{\text{DM},0} = 0.259$, $\Omega_{\text{m}0} = 0.307$, and $\Omega_{\Lambda,0} = 0.693$.

2 THE DOUBLE LENS CONFIGURATION

We examine the distortion of a (razor-thin) lensing arc due to the presence of a perturbing black hole along the line of sight. We refer to the massive, primary lens that gives rise to the arc as the lens (L) and to the black hole as the perturber (P). If P is located sufficiently close to the geodesic connecting source (S) and observer (O), its gravitational lensing can cause a significant, localized perturbation of the arc, which is the signature we are considering here. In particular, we aim to compute the effective volume, centred around this geodesic, inside of which a perturbing black hole of a given mass, M_P , causes such a detectable distortion.

The lens and the perturber are generally located at different redshifts. If they reside at the same redshift, the overall deflection of light from the source due to the combined effect of the two lenses is simply the sum of the deflections caused by L and P. However, in the case that the two are located at different redshifts, the overall angle of deflection is determined by the double lens equation (Schneider et al. 1992; Keeton 2003), which is the equation we use throughout. Note that the perturber can be either in the foreground (between the lens and observer) or in the background (between the source and lens). Both configurations are depicted in Fig. 1, which specifies the various angles and distances used throughout.

We use D_S , D_L , and D_P to refer to the (physical) angular diameter distances from the observer to the source, the lens, and the perturber, respectively. D_{PS} and D_{LS} indicate the angular diameter distances from P to S and L to S, respectively. Here,

$$D_{12} \equiv \frac{r_{12}}{1 + z_2}, \quad (1)$$

where r_{12} is the comoving distance between two objects along the same line of sight located at redshifts z_1 and $z_2 > z_1$ (e.g. Mo, van den Bosch & White 2010). Finally, D_{PL} indicates the angular diameter distance from the perturber to the lens in the foreground configuration (depicted in Fig. 1a), while D_{LP} stands for the same from the lens to the perturber in the background (depicted in Fig. 1b) configuration.

2.1 Foreground configuration

First let us consider the foreground configuration depicted in Fig. 1(a). Let $\vec{\theta}$ be the angle between the image, I, and the line OL (hereafter ‘baseline’), joining the main lens (located at redshift z_L) and observer. Let $\vec{\alpha}_{\text{DL}}$ and $\vec{\alpha}_{\text{DP}}$ be the angles of deflection due to the lens and the perturber subtended at the lens and the perturber, respectively, and let $\vec{\alpha}_L$ and $\vec{\alpha}_P$ be the corresponding deflection angles subtended at the observer. These are related according to

$$\vec{\alpha}_L = \frac{D_{LS}}{D_S} \vec{\alpha}_{\text{DL}}, \quad \vec{\alpha}_P = \frac{D_{PS}}{D_S} \vec{\alpha}_{\text{DP}}. \quad (2)$$

Finally, we define $\vec{\beta}_S$ and $\vec{\beta}_P$ as the angles between the baseline, OL, and the lines of sight towards S and P, respectively.

When the perturber is present, the double lens equation describing the system can be written as

$$\vec{\beta}_S = \vec{\theta} - \vec{\alpha}_P(\vec{\theta}) - \vec{\alpha}_L(\vec{\theta}'). \quad (3)$$

Here,

$$\vec{\theta}' = \vec{\theta} - \gamma_f \vec{\alpha}_L(\vec{\theta}) \quad (4)$$

with

$$\gamma_f \equiv \frac{D_{PL}}{D_L} \frac{D_S}{D_{PS}}. \quad (5)$$

In absence of the perturber, the lens equation reduces to

$$\vec{\beta}_S = \vec{\theta}_0 - \vec{\alpha}_L(\vec{\theta}_0), \quad (6)$$

where $\vec{\theta}_0$ is the image angle in absence of the perturber.

Subtracting equation (3) from equation (6) and expanding perturbatively to linear order around $\vec{\theta}_0$, we obtain

$$\delta\vec{\theta} \equiv \vec{\theta} - \vec{\theta}_0 = \left(1 - \vec{\nabla}_{\vec{\theta}} \vec{\alpha}_L(\vec{\theta}_0)\right)^{-1} \left(1 - \gamma_f \vec{\nabla}_{\vec{\theta}} \vec{\alpha}_L(\vec{\theta}_0)\right) \vec{\alpha}_P(\vec{\theta}). \quad (7)$$

This perturbative form of the lens equation can be solved numerically² for the distortion, $\delta\vec{\theta}$, due to the perturber P.

2.2 Background configuration

If the perturbing black hole is located in the background (i.e. between the primary lens and the source; see Fig. 1b), the double lens equation is of the form

$$\vec{\beta}_S = \vec{\theta} - \vec{\alpha}_L(\vec{\theta}) - \vec{\alpha}_P(\vec{\theta}'). \quad (8)$$

Here,

$$\vec{\theta}' = \vec{\theta} - \gamma_b \vec{\alpha}_L(\vec{\theta}), \quad (9)$$

with

$$\gamma_b \equiv \frac{D_{LP}}{D_P} \frac{D_S}{D_{LS}}. \quad (10)$$

Subtracting equation (8) from equation (6) and expanding perturbatively to linear order around $\vec{\theta}_0$, now yields

$$\delta\vec{\theta} = \left(1 - \vec{\nabla}_{\vec{\theta}} \vec{\alpha}_L(\vec{\theta}_0)\right)^{-1} \vec{\alpha}_P(\vec{\theta}'). \quad (11)$$

²To numerically solve the perturbative form of the lens equation, we use the SCIPY (Jones et al. 2001) module `fsolve`, which is a wrapper around MINPACK’s `hybrd` and `hybrj` algorithms. Both find the roots of a system of N non-linear equations with N variables using a modified form of the Powell hybrid method (Powell 1970).

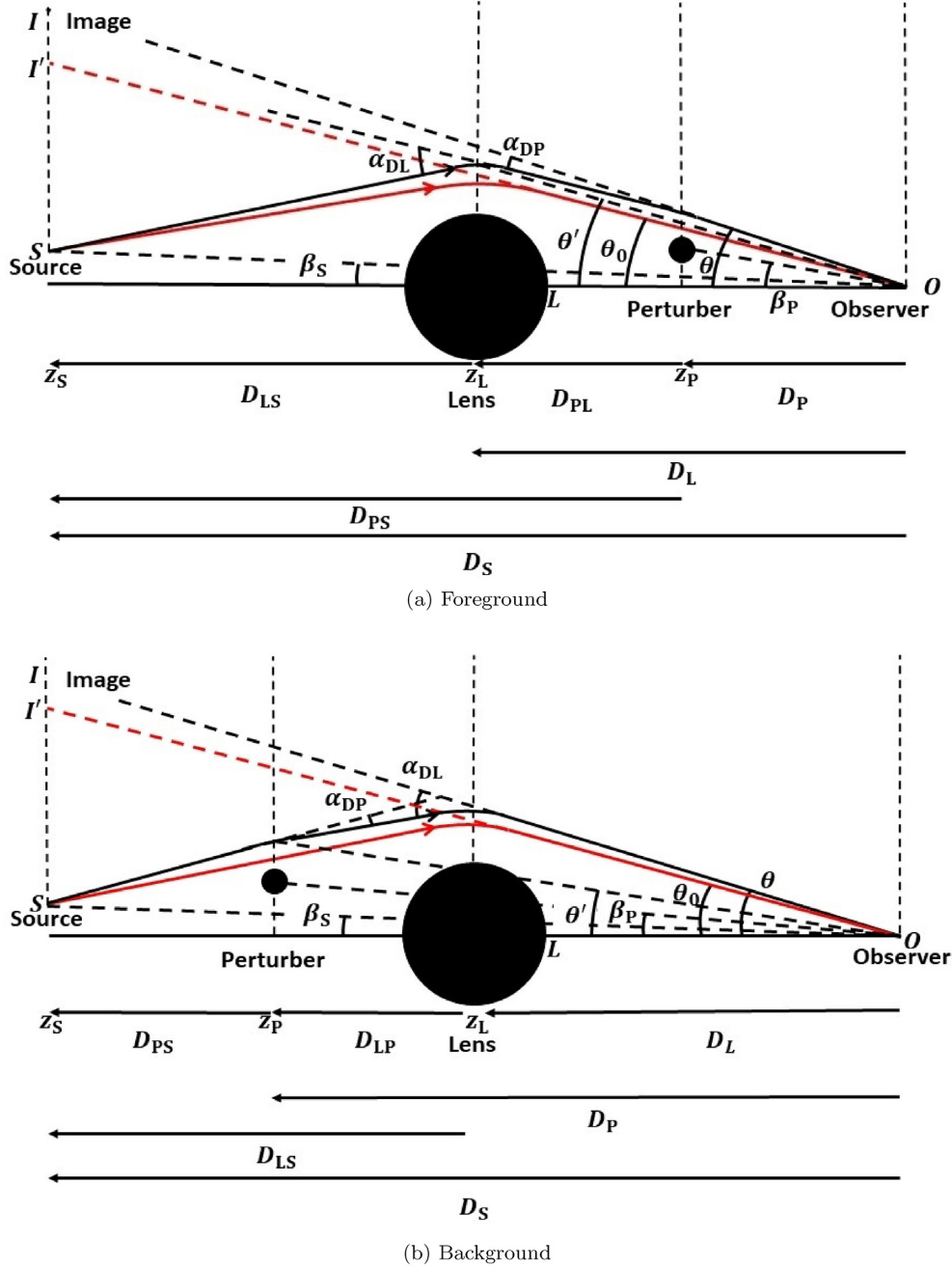


Figure 1. Schematic of the foreground and background double lensing configurations as viewed from the side. The black and red rays denote the perturbed and unperturbed geodesics, respectively. Only one component of the angles is shown.

2.3 Matrix notation

It is useful to write the above expressions for the distortion $\delta\vec{\theta}$ in matrix notation:

$$\delta\vec{\theta} = \begin{cases} \mathbf{M}(\vec{\theta}_0) & \mathbf{C}(\vec{\theta}_0) & \vec{\alpha}_P(\vec{\theta}), & \text{foreground,} \\ \mathbf{M}(\vec{\theta}_0) & \vec{\alpha}_P(\vec{\theta}'), & & \text{background.} \end{cases} \quad (12)$$

Here, $\mathbf{M}(\vec{\theta}_0) = (1 - \vec{\nabla}_\theta \vec{\alpha}_L(\vec{\theta}_0))^{-1}$ is the magnification tensor for the lens, and $\mathbf{C}(\vec{\theta}_0) = (1 - \gamma_f \vec{\nabla}_\theta \vec{\alpha}_L(\vec{\theta}_0))$ is the correction tensor for the double lens configuration.

Throughout we define a Cartesian basis in which the y-axis connects the perturber to the baseline, and the x-axis is perpendicular to both the baseline and the y-axis. In this basis, the x-component of $\vec{\beta}_P$ is zero by construction,

$$\delta\vec{\theta} = \begin{bmatrix} \delta\theta_x \\ \delta\theta_y \end{bmatrix}, \quad (13)$$

and the magnification and correction tensors are given by

$$\mathbf{M}(\vec{\theta}_0) = \frac{1}{1 - \frac{\theta_E}{\theta_0}} \begin{bmatrix} 1 - \theta_E \frac{\theta_{0x}^2}{\theta_0^3} & -\theta_E \frac{\theta_{0x}\theta_{0y}}{\theta_0^3} \\ -\theta_E \frac{\theta_{0x}\theta_{0y}}{\theta_0^3} & 1 - \theta_E \frac{\theta_{0y}^2}{\theta_0^3} \end{bmatrix}, \quad (14)$$

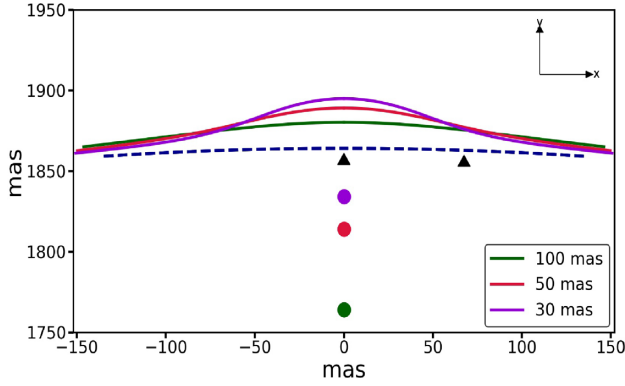


Figure 3. Perturbed arc in presence of a $10^7 M_\odot$ perturber at $z_P = 0.01$ for the fiducial case ($z_L = 0.881$, $z_S = 2.056$, $M_L(\theta_E) = 10^{12} M_\odot$, and $|\beta_S| = 36$ mas, i.e. $|\theta_0| = 1.866$ arcsec), obtained by numerically solving the perturbative form of the double lens equation (12). The blue dashed line indicates the unperturbed arc and the coloured solid lines indicate the perturbed arcs for three different angular impact parameters of the perturber (green: 100 mas, red: 50 mas, violet: 30 mas) defined with respect to the unperturbed arc. The black arrows indicate the points on the arc pertaining to the detectability criteria (see equation 22). Note that for each angular impact parameter only one of the two perturbed arcs is shown here.

Throughout this paper, we shall define the ‘detectability’ of the perturber based purely on this geometrical, kink-like distortion, without taking account of how the perturber magnifies or demagnifies the light along the arc. We focus exclusively on kink-like distortions that are easily detectable ‘by eye’, by which we mean, without any sophisticated analysis. For this to be the case the magnitude of the distortion needs to be both sufficiently large (compared to the resolution of the data), and sufficiently local or ‘kink’-like. The magnitude of the distortion can be quantified in terms of the magnitude of the vector $\delta\vec{\theta}_1$ in Fig. 2, i.e. the magnitude of the radial distortion at the point closest to the black hole. The importance of the second, ‘locality’ criterion is obvious from considering the green curve in Fig. 3: although in this case $|\delta\vec{\theta}_1|$ may be significantly larger than the spatial resolution of the data, \mathcal{R} , the distortion is not particularly ‘localized’. This owes its origin to the fact that the tangential component of the distortion vector, $\delta\vec{\theta}$, can become much larger than the radial component. If that is the case, the distortion may elude detection because it will be difficult to tell such a distortion apart from the effect of external shear, or a small modification of the (shape of) the main lens.

In order to assure that the perturbation is sufficiently localized, we therefore quantify the detectability in terms of the *difference* in the radial perturbations at two points along the arc. Those two points include the point on the arc closest to the perturbing black hole and another point separated by an angular distance of $f\omega_{\text{arc}}/2$ along the arc, where $0 < f < 1$ is a free parameter. As long as this difference in the radial distortion is sufficiently large compared to the spatial resolution of the data, the perturber’s presence will be detectable by eye from a localized, kink-like distortion in the razor-thin arc. Hence, our detectability criterion is given by

$$\Delta\theta_r \equiv \delta\theta_r(\vec{\theta}_1) - \delta\theta_r(\vec{\theta}_2) \geq \mathcal{R}/2, \quad (22)$$

where the indices 1 and 2 refer to the two points along the arc; point 1 is located closest to the perturber where the radial distortion is the largest, and point 2 is offset from point 1 by an angle $f\omega_{\text{arc}}/2$ along the arc (see Fig. 3). Throughout, we adopt $f = 0.5$ as our fiducial

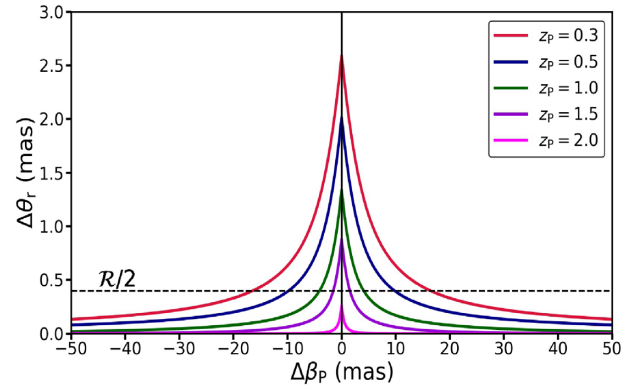


Figure 4. Angular distortion of our fiducial lensing arc, quantified in terms of $\Delta\theta_r$ as a function of angular impact parameter, $\Delta\beta_P$, for a perturbing black hole of mass $M_P = 10^6 M_\odot$. Results are shown for five different redshifts of the perturber (red and blue in the foreground and the rest in the background), as indicated. The dotted, horizontal line indicates the detection threshold, $\mathcal{R}/2$, where we adopt our fiducial, spatial resolution of $\mathcal{R} = 0.8$ mas. The perturbation is deemed detectable whenever the curve is above this threshold, i.e. when $\Delta\theta_r > \mathcal{R}/2$. This occurs for a finite range of angular impact parameters, $|\Delta\beta_P| < \Delta\beta_{P,\text{max}}$. Note that $\Delta\beta_{P,\text{max}}$ decreases with increasing redshift of the perturber and that the maximum distortion (which occurs for zero impact parameter and is equal to the Einstein angle of the perturber) falls below the detection limit beyond a certain redshift.

value. As we demonstrate in Section 5.1, our results only depend very weakly on this choice.

For given redshifts of source, lens, and perturber, the distortion quantified in terms of $\Delta\theta_r$ becomes larger with increasing black hole mass, M_P , and decreasing impact parameter b_0 , defined as the distance in the lens plane of the perturber between the perturber and the unperturbed geodesic between source and observer, i.e.

$$b_0 \equiv D_P \Delta\beta_P = \begin{cases} D_P (|\vec{\theta}_0| - \beta_P), & \text{foreground,} \\ D_P (|\vec{\theta}_0| + \beta_P), & \text{background,} \end{cases} \quad (23)$$

where $|\vec{\theta}_0| = |\vec{\theta}_0| - \gamma_b \theta_E$, and we have defined the corresponding *angular* impact parameter, $\Delta\beta_P$.

Fig. 4 plots the distortion, $\Delta\theta_r$, for our fiducial lensing configuration (Section 2.5) as a function of the angular impact parameter, $\Delta\beta_P$, computed using equations (12) and (17) for a perturber mass of $M_P = 10^6 M_\odot$. The different curves correspond to different redshifts for the perturber (two in the foreground and three in the background), as indicated, while the dashed, horizontal line corresponds to a fiducial spatial resolution of $\mathcal{R}/2 = 0.4$ mas. Placing the perturbing black hole at a smaller redshift results in a larger distortion, and hence in a wider range of the angular impact parameter for which $\Delta\theta_r > \mathcal{R}/2$. This is because the Einstein radius of the perturber decreases with increasing redshift.

At given redshifts for source, lens, and perturber, the condition for detectability translates into a required range for the angular impact parameter,

$$\Delta\beta_P \leq \Delta\beta_{P,\text{max}}, \quad (24)$$

where $\beta_{P,\text{max}}$ corresponds to the angular impact parameter for which $\Delta\theta_r = \mathcal{R}/2$. Note that a sufficiently small perturber may never satisfy the detectability condition stated in equation (22), even for zero impact parameter. In fact, to each perturber redshift, $0 \leq z_P \leq z_S$, corresponds a minimum detectable perturber mass, $M_{P,\text{min}}$, or, equivalently, with each perturber mass M_P , corresponds a max-

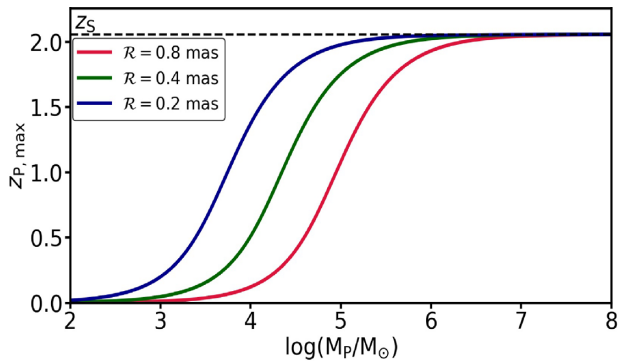


Figure 5. Maximum redshift out to which kink-like distortions of our fiducial arc due to a perturbing black hole are detectable as a function of the black hole mass M_P . Different colours correspond to different spatial resolutions, as indicated. The maximum redshift for detectability increases with black hole mass and tends towards the source redshift for sufficiently massive black holes. Also note that it increases for higher spatial resolution.

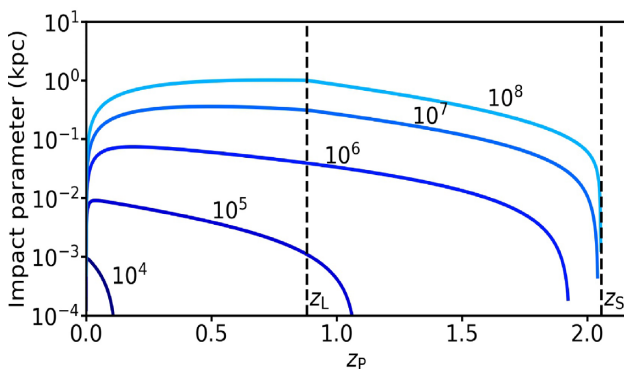


Figure 6. Maximum impact parameter for which a perturbing black hole causes a detectable distortion of our fiducial arc. Results are shown as a function of the redshift of the perturber, z_P , and for five different perturber masses, as indicated. The maximum impact parameter increases with perturber mass but initially increases and then decreases with perturber redshift. Note that the maximum redshift out to which a perturbing black hole can be detected increases with black hole mass, and approaches the source redshift for $M_P \gtrsim 10^7 M_\odot$.

imum redshift, $0 \leq z_{P,\max} \leq z_S$, out to which such a perturber can be detected. Beyond that redshift even the maximum value of $\Delta\theta_r$, which occurs for $\Delta\beta_P = 0$ and is equal to θ_{EP} , falls below the detection limit $\mathcal{R}/2$. Therefore, the maximum redshift of detectability, $z_{P,\max}$, can be obtained as the root for z_P of $\theta_{EP}(z_P) = \mathcal{R}/2$. The red line in Fig. 5 plots $z_{P,\max}$ as a function of M_P for our fiducial lens configuration. It increases from close to zero for $M_P < 10^3 M_\odot$ to roughly z_S for $M_P > 10^7 M_\odot$. Hence, free-floating black holes less massive than $\sim 10^3 M_\odot$ are never detectable (according to our detectability criterion), while those with $M_P \gtrsim 10^7 M_\odot$ are detectable at all redshifts between observer and source. The green and blue curves show the behaviour for $\mathcal{R} = 0.4$ and 0.2 mas, respectively. As expected, the maximum redshift of detectability increases with better spatial resolution (smaller \mathcal{R}).

Fig. 6 plots the maximum impact parameter, $b_{0,\max} = D_P \Delta\beta_{P,\max}$, as a function of the redshift of the perturbing black hole, z_P , for our fiducial lensing configuration. Different curves correspond to different black hole masses, as indicated. Note how perturbing black holes with mass $M_P \lesssim 10^7 M_\odot$ can only be detected out to a redshift

$z_{P,\max} < z_S$ (cf. Fig. 5). One can also see from Fig. 6 that $b_{0,\max}$ increases with higher perturber mass.

As already eluded to above, our detectability criterion is based solely on the geometric distortion $\delta\theta$, without recourse to the magnification caused by the perturber. In order to have an idea as to the potential impact of magnification, we have used GRAVLENS (Keeton 2001) to make mock images of our fiducial razor-thin arc, being perturbed by a black hole of mass $M_P = 10^6 M_\odot$ at a redshift of $z_P = 0.5$. The resulting images, for a spatial resolution of 0.8 mas, are shown in Fig. 7. From left to right, the different panels correspond to angular impact parameters of $\Delta\beta_P = -3.2, -1.6$, and 0 mas. The left and middle panels reveal local, kink-like distortions similar to what is shown in Fig. 3. In addition, the perturber creates a small, second arclet opposite to the kink, which is a feature that we ignore throughout this paper. When the perturber exactly aligns with the arc, as in the right-hand panel, a small Einstein ring is visible. Upon close inspection of these images, it is evident that the perturber causes some magnification/demagnification of parts of the arc close to the distortion, but overall it is clear that the main characteristic of the distortion is its kink-like geometry, not the corresponding (de)magnification. This justifies the use of our detectability criterion (22). In fact, by focusing only on the geometric distortion, our constraints will be conservative, i.e. a sophisticated analysis of the surface brightness variations along the arc, similar to the analyses of strong-lensing distortions by Vegetti et al. (2014), Hezaveh et al. (2016b), or Birrer et al. (2017), might allow the detection of even lower-mass perturbers due to their localized (de)magnification of the arc.

We point out that throughout we assume the main lens to be spherically symmetric. In general, the shape of the kink might change, and the kink itself might be more difficult to identify ‘by eye’, if the main lens is strongly elliptical or if external shear is present. This could potentially make the approach presented here less effective. However, in general such extreme configurations would also disrupt the arc, splitting it in multiple images, and thus leading to a different type of lensing configuration. Hence, given that this is only a fairly crude analysis, based on distortions that are easily identifiable ‘by eye’, and given that only a handful of systems have been observed yet at milliarcsecond resolution, we consider the influence of ellipticity and shear to be higher-order effects that only warrant careful consideration when the quantity and quality of the data improve.

Finally, we emphasize that the localized kink-like distortions considered here must arise from extremely compact objects, such as the black holes. They cannot be caused by perturbations due to the (far more abundant) dark matter haloes along the line of sight. Although dark matter haloes (or subhaloes) can perturb gravitational lensing arcs (see e.g. Koopmans 2005; More et al. 2009; Vegetti & Koopmans 2009; Vegetti et al. 2010, 2012; Hezaveh et al. 2016b; Birrer et al. 2017), we demonstrate in Appendix B that such perturbations are not sufficiently localized to be detectable according to our criterion (22).

4 TOWARDS CONSTRAINTS ON THE COMOVING NUMBER DENSITY OF FREE-FLOATING BLACK HOLES

Our aim in this paper is to translate the presence of kink-like distortions along razor-thin lensing arcs, or the absence thereof, into constraints on the number density of black holes; either primordial ones or wandering black holes that were formed as a by-product of galaxy formation (see Section 1). In the previous two sections, we have shown how to compute the angular extent of such a kink-like

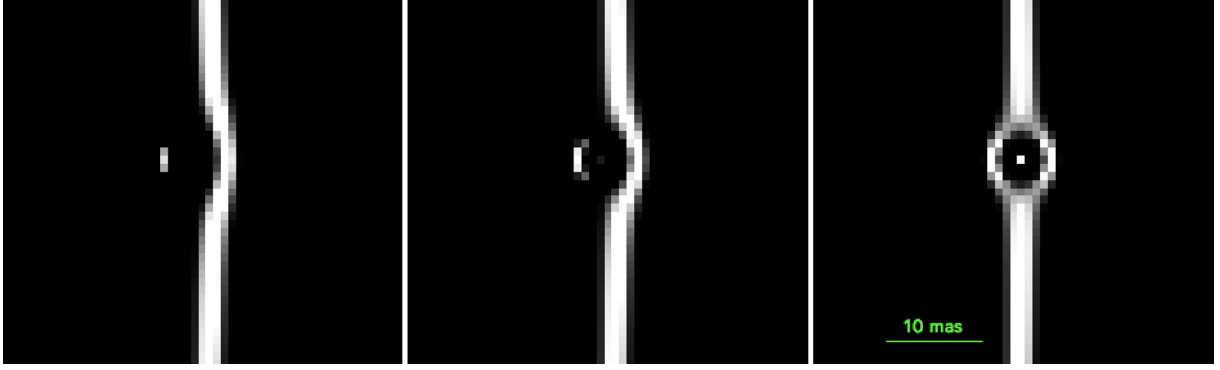


Figure 7. Mock (noiseless) images constructed using GRAVLENS (Keeton 2001) of the distortions caused in a razor-thin lensing arc due to a perturbing BH of mass $M_P = 10^6 M_\odot$ at $z_P = 0.5$ along the line of sight. The images have been obtained by boxcar filtering with an FWHM of 0.8 mas. An arc ~ 270 mas long is formed due to the gravitational lensing of a source at $z_S = 2.056$ by a singular isothermal sphere with a mass of $\sim 10^{12} M_\odot$ within the Einstein radius (≈ 2 arcsec) and located at a redshift $z_L = 0.881$. The source is assumed to have a Sérsic profile and is aligned at an angle of 36 mas from the baseline. The radius of the unperturbed arc is ≈ 2.036 arcsec that is equivalent to 2545 pixels (each pixel $\equiv 0.8$ mas) in this image. The different columns from left to right correspond to different angular impact parameters ($\Delta\beta_P$) of -3.2 , -1.6 , and 0 mas with respect to the unperturbed arc. Note how the BH causes a kink-like distortion in the arc, which is easily detectable ‘by eye’, given the resolution of the images, and in the absence of noise.

distortion, $\Delta\theta_r$, for a given lensing configuration and a given black hole mass, and we have shown that the criterion for detectability translates into a constraint on the maximum (angular) impact parameter of the black hole with respect to the unperturbed geodesic from the source to the observer. We now show how a given number of kink-like distortions, N_{dis} , for a lensing arc of length ω_{arc} , translates into a constraint on the comoving number density of black hole perturbers, n_{BH} . For the sake of simplicity, we ignore potential evolution in n_{BH} with redshift, but that is easily accounted for.

If we assume, for simplicity, that the number of free-floating black holes of mass M_{BH} in a given comoving volume, V , follows a Poisson distribution with mean $\lambda = n_{\text{BH}}(M_{\text{BH}}) V$, then the detection of N_{dis} distortions along an arc specified by z_S , z_L , ω_{arc} , and \mathcal{R} implies the following 95 per cent confidence interval on $n_{\text{BH}}(M_{\text{BH}})$:

$$\frac{\lambda_{\text{lower}}}{V_{\text{eff}}(M_{\text{BH}})} \leq n_{\text{BH}}(M_{\text{BH}}) \leq \frac{\lambda_{\text{upper}}}{V_{\text{eff}}(M_{\text{BH}})}. \quad (25)$$

Here, V_{eff} is the effective volume inside of which a perturbing black hole of mass M_{BH} can be detected through its kink-like distortion of the arc, which is given by

$$V_{\text{eff}}(M_P) = \int_0^{z_S} \Omega(z) \frac{d^2 V}{d\Omega dz} dz. \quad (26)$$

Here, $d^2 V / (d\Omega dz)$ is the comoving volume element at redshift z corresponding to a solid angle $d\Omega$ and a redshift depth dz , and the solid angle $\Omega(z)$, in the small angle approximation, is given by

$$\Omega(z) \approx 2\omega_{\text{arc}} \Delta\beta_{P,\text{max}}(z). \quad (27)$$

The factor of 2 accounts for the fact that the perturber may reside on either side of the arc, and the angular impact parameter $\Delta\beta_{P,\text{max}}(z)$ follows from our detection criterion (equation 22) and the double lens equations presented in Sections 2.1 and 2.2. Note that $\Omega(z) = 0$ for $z > z_{P,\text{max}}$. The total effective volume V_{eff} can be split into the foreground and background volumes, which we compute separately and then add up.

The $1 - \mathcal{C}$ confidence interval on λ is given by

$$\lambda_{\text{lower}} \equiv \frac{1}{2} \chi^2(\mathcal{C}/2, 2N_{\text{dis}}), \quad (28)$$

Table 1. Two-sided confidence intervals (λ_{lower} , λ_{upper}) for the mean of a Poisson distribution given N_{dis} detections. We list results for $N_{\text{dis}} = 0, 1, \dots, 5$ and for confidence levels of 68 per cent ($\lambda_{0.160}$, $\lambda_{0.840}$), 95 per cent ($\lambda_{0.025}$, $\lambda_{0.975}$), and 99 per cent ($\lambda_{0.005}$, $\lambda_{0.995}$).

N_{dis}	λ_{lower}		λ_{upper}			
	$\lambda_{0.005}$	$\lambda_{0.025}$	$\lambda_{0.160}$	$\lambda_{0.840}$	$\lambda_{0.975}$	$\lambda_{0.995}$
0	0.00	0.00	0.00	1.83	3.69	5.30
1	0.01	0.03	0.17	3.29	5.57	7.43
2	0.10	0.24	0.71	4.62	7.22	9.27
3	0.34	0.62	1.37	5.90	8.77	10.98
4	0.67	1.09	2.09	7.15	10.24	12.59
5	1.08	1.62	2.85	8.37	11.67	14.15

and

$$\lambda_{\text{upper}} \equiv \frac{1}{2} \chi^2(1 - \mathcal{C}/2, 2N_{\text{dis}} + 2), \quad (29)$$

where $\chi^2(p; n)$ is the quantile function of the χ^2 -distribution with n degrees of freedom (Garwood 1936). Values for λ_{lower} and λ_{upper} have to be computed numerically or taken from look-up tables. For easy reference, Table 1 lists λ_{lower} and λ_{upper} for $N_{\text{dis}} = 0, 1, 2, \dots, 5$ and for confidence levels of $\mathcal{C} = 0.32, 0.05$, and 0.01 . Note that in the absence of any detections ($N_{\text{dis}} = 0$), we only obtain an upper limit on the number density of black holes; at 95 per cent (99 per cent) confidence, a null-detection implies that $n_{\text{BH}}(M_{\text{BH}}) V_{\text{eff}}(M_{\text{BH}}) < 3.69$ (5.30).

The above applies to the constraints that result from a single arc. When multiple arcs have been observed, the constraint on $n_{\text{BH}}(M_{\text{BH}})$ simply follows from adding the effective volumes and distortions of the individual arcs, that is, from using equations (25)–(29) with $V_{\text{eff}} \rightarrow V_{\text{eff,tot}} = \sum_{i=1}^{N_{\text{arc}}} V_{\text{eff},i}$ and $N_{\text{dis}} \rightarrow N_{\text{dis,tot}} = \sum_{i=1}^{N_{\text{arc}}} N_{\text{dis},i}$.

5 RESULTS

In this section, we discuss various constraints on the number and mass densities of free-floating black holes that one may realistically achieve with observations of our fiducial razor-thin arc.

5.1 Constraints for single-mass species

We start by considering the case in which all free-floating black holes have the same mass, M_{BH} . Under the assumption of no detected distortions (i.e. $N_{\text{dis}} = 0$), we obtain an upper limit on the mass density of such black holes, n_{BH} , which we express in terms of $\Omega_{\text{BH}}/\Omega_{\text{DM},0}$. Here, $\Omega_{\text{DM},0}$ is the assumed dark matter density in units of the critical density, for which we adopt $\Omega_{\text{DM},0} = 0.259$ (Planck Collaboration XVI 2014), and $\Omega_{\text{BH}} = M_{\text{BH}} n_{\text{BH}}/\rho_{\text{crit}}$.

The solid lines in Fig. 8 show the constraints on $\Omega_{\text{BH}}/\Omega_{\text{DM}}$ that we obtain as a function of the black hole mass M_{P} for different resolutions (left-hand panel), different source redshifts (middle panel), and different values of the parameter f (right-hand panel). In each panel, the red curve corresponds to our fiducial configuration. The constraints on $\Omega_{\text{BH}}/\Omega_{\text{DM}}$ are most stringent for intermediate black hole mass with $M_{\text{P}} \sim 10^6 M_{\odot}$. The constraints improve with higher spatial resolution (i.e. smaller \mathcal{R}), especially at the low-mass end, with increasing source redshift, z_{S} , and depend only weakly on the parameter f that regulates the angular distance along the arc at which we compare the angular distortion, $\delta\theta_r$. The trend with z_{S} is easy to understand from the fact that the effective volume increases with increasing z_{S} . Similarly, decreasing \mathcal{R} and increasing f make our detectability criterion (22) less strict, thereby resulting in a stronger constraint on $\Omega_{\text{BH}}/\Omega_{\text{DM}}$. Note that the constraints on $\Omega_{\text{BH}}/\Omega_{\text{DM}}$ get tighter with increase in the arc length probed, ω_{arc} , i.e. as more razor-thin arcs are observed.

In Appendix A, we derive how our constraints scale with the mass of the perturber, M_{P} , and with the spatial resolution, \mathcal{R} , by analytically solving the perturbative form of the double lens equation (12) in the small and large mass limits. In particular, we show that for massive perturbers, which have a mass well in excess of a characteristic mass scale

$$M_0 \equiv \frac{\mathcal{R}^2 c^2}{16 G} D_{\text{S}} \simeq 3 \times 10^4 M_{\odot} \left(\frac{\mathcal{R}}{\text{mas}} \right)^2 \left(\frac{D_{\text{S}}}{\text{Gpc}} \right), \quad (30)$$

the effective volume (equation 26) scales as

$$V_{\text{eff}} \propto (\omega_{\text{arc}})^{\frac{5}{3}} \left(\frac{M_{\text{P}}}{\mathcal{R}} \right)^{\frac{1}{3}}. \quad (31)$$

Since $\Omega_{\text{BH}} \propto \rho_{\text{BH}} \propto M_{\text{BH}}/V_{\text{eff}}$, the constraint on $\Omega_{\text{BH}}/\Omega_{\text{DM}}$ for a given number of detections, N_{dis} , scales as

$$\Omega_{\text{BH}}/\Omega_{\text{DM}} \propto M_{\text{P}}^{\frac{2}{3}} \mathcal{R}^{\frac{1}{3}} \frac{N_{\text{dis}}}{(\omega_{\text{arc}})^{\frac{5}{3}}}. \quad (32)$$

For perturbers with a mass $M_{\text{P}} \ll M_0$, the effective volume scales as

$$V_{\text{eff}} \propto \omega_{\text{arc}} \frac{M_{\text{P}}^3}{\mathcal{R}^5}, \quad (33)$$

which implies that

$$\Omega_{\text{BH}}/\Omega_{\text{DM}} \propto \frac{1}{\omega_{\text{arc}}} \frac{\mathcal{R}^5}{M_{\text{P}}^2} N_{\text{dis}}. \quad (34)$$

Hence, the constraint on $\Omega_{\text{BH}}/\Omega_{\text{DM}}$ becomes much weaker for lower mass black holes. Note, though, that the constraining power depends extremely strongly on the spatial resolving power in this limit. Increasing the spatial resolution by a factor of 2 will improve the constraints on $\Omega_{\text{BH}}/\Omega_{\text{DM}}$ (for $M_{\text{P}} \ll M_0$) by a factor of 32. In addition, the characteristic turnover mass M_{TO} (see equation A19 of Appendix A) that scales as $\mathcal{R}^{7/4}$ reduces by a factor of ≈ 3.4 that further improves the constraining power.

It is informative to compare these constraints from a null-detection along our fiducial arc to existing constraints. The shaded

regions in Fig. 8 show such constraints³ from quasar milli-lensing (Wilkinson et al. 2001), the survival of a star cluster in Eridanus II (Brandt 2016), wide binary stability against tidal disruption by black holes (Quinn & Smith 2009), generation of large-scale structure through Poisson fluctuations and its imprint on Ly α clouds (Afshordi et al. 2003), and WMAP constraints on the accretion effects of PBHs on the CMB (Ricotti et al. 2008). The WMAP and Ly α constraints apply exclusively to PBHs, whereas the other constraints from milli-lensing and dynamical effects apply to all black holes independent of their formation epoch.

Clearly, the constraints from a potential null-detection along our fiducial razor-thin arc are not particularly competitive. For the fiducial redshifts of the source and the lens, and for a fiducial resolution of $\mathcal{R} = 0.8$ mas, the constraints are comparable to those from the quasar milli-lensing constraints of Wilkinson et al. (2001), which derive from the absence of multiple images (at mas resolution) among a sample of 300 compact radio sources. These constraints, though, are much weaker than the constraints (on PBHs) that derive from WMAP or Ly α data. In order for distortions of razor-thin arcs to yield constraints that are competitive with these data we require a sample of hundreds to thousands of razor-thin arcs, preferentially at high spatial resolution, and with high-redshift sources.

5.2 Constraining the mass function of wandering black holes

We now consider the more realistic case, in which the free-floating black holes are characterized by a mass function. In the case of PBHs, it is unclear what the mass function will be; depending on the exact formation mechanism and epoch, the mass function can be either extended or very narrow (see discussion in Carr et al. 2016). In the case of wandering black holes, though, we may use the notion that they are a by-product of galaxy formation to argue that they should (roughly) follow a Schechter mass function,

$$\frac{dn}{dM_{\text{BH}}} dM_{\text{BH}} = n_{\text{BH}}^* \left(\frac{M_{\text{BH}}}{M_{\text{BH}}^*} \right)^{\alpha} \exp \left(-\frac{M_{\text{BH}}}{M_{\text{BH}}^*} \right) \frac{dM_{\text{BH}}}{M_{\text{BH}}^*}. \quad (35)$$

After all, the galaxy stellar mass function is well described by a Schechter function, and the masses of SMBHs at the centres of galaxies are tightly correlated with bulge mass (Marconi & Hunt 2003; Häring & Rix 2004). Using that the most massive galaxies have SMBHs of mass $M_{\text{BH}} \sim 10^9 M_{\odot}$, we adopt a characteristic black hole mass of $M_{\text{BH}}^* = 10^9 M_{\odot}$. Above this mass scale the abundance of wandering black holes is exponentially suppressed, while the mass function follows a simple power law, with index α , for $M \ll M_{\text{BH}}^*$. The characteristic, comoving number density, n_{BH}^* sets the overall normalization.

To demonstrate that the Schechter function is adequate, Fig. 9 plots the mass function of wandering black holes in the ROMULUS25 simulation (solid dots). The dashed line is the best-fitting Schechter mass function with $M_{\text{BH}}^* = 10^9 M_{\odot}$, which accurately fits that data. The resulting best-fitting slope and normalization are $\alpha = -2.22$ and $n_{\text{BH}}^* = 3.11 \times 10^{-5} \text{ Mpc}^{-3}$. Note that the slope is steeper than -2 , which implies that the mass density of wandering black holes in the ROMULUS25 simulation is dominated by the least massive ones. However, ROMULUS25 adopts a black hole seed mass of $10^6 M_{\odot}$, and the results shown in Fig. 9 are likely affected by this choice. We therefore caution that the predicted slope is likely to change with a

³To not clutter Fig. 8, the constraints shown are not exhaustive; see Carr & Silk (2018) for a few additional constraints in the mass range shown.

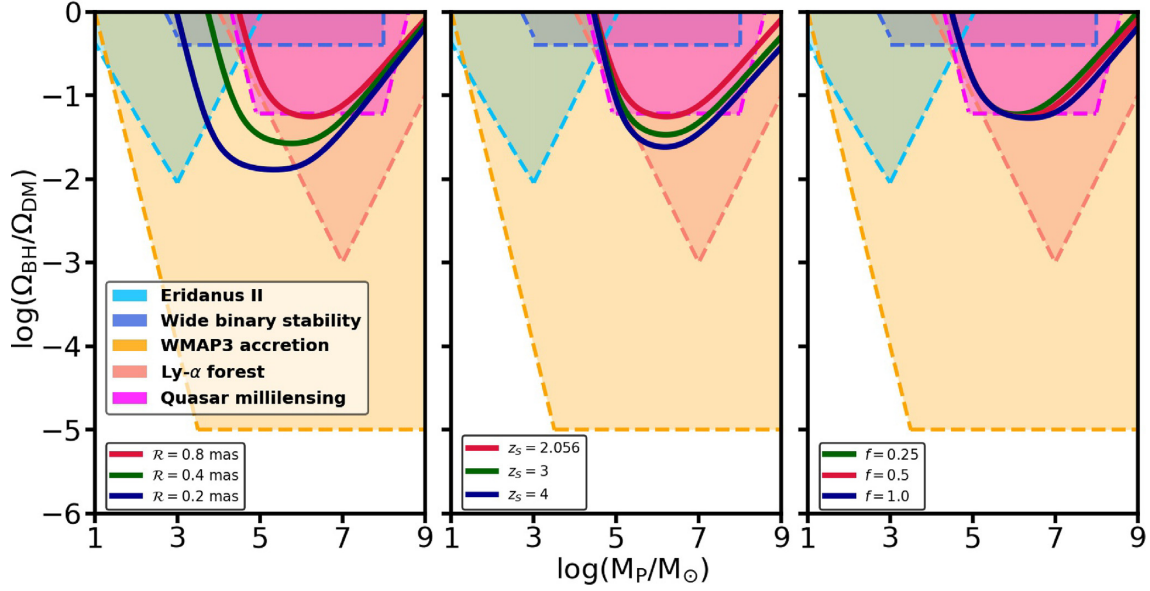


Figure 8. Single null detection: maximum constraint on the ratio of the mean comoving mass density of free-floating black holes (considered as PBHs) to the dark matter comoving density expressed as $\Omega_{\text{BH}}/\Omega_{\text{DM}}$ versus black hole mass M_P in units of M_\odot for different values of \mathcal{R} , z_s , and f ($M_L = 10^{12} M_\odot$, $\omega_{\text{arc}} = 270$ mas, $z_L = 0.881$) at 95 per cent confidence level. The constraints in general are the tightest at some intermediate black hole mass the value of which depends on the spatial resolution \mathcal{R} with which the arc is probed. Also shown are the previously obtained constraints (shaded regions are ruled out) on $\Omega_{\text{BH}}/\Omega_{\text{DM}}$ for PBHs. From the left panel, it can be seen that the constraints get tighter and the characteristic black hole mass (turnover mass) gets reduced for higher spatial resolution. In the near future, with the discovery of more finely resolved lensing arcs, it will be possible to put constraints on the unconstrained regions of the plot, i.e. in the mass range $M_P \lesssim 10^3 M_\odot$. Also shown are existing constraints from quasar milli-lensing (Wilkinson et al. 2001), the survival of a star cluster in Eridanus II (Brandt 2016), wide binary stability (Quinn & Smith 2009), the impact of Poisson noise in the matter power spectrum on the Ly α forest (Afshordi, McDonald & Spergel 2003), and WMAP3 constraints on accretion on to black holes prior to recombination (Ricotti et al. 2008).

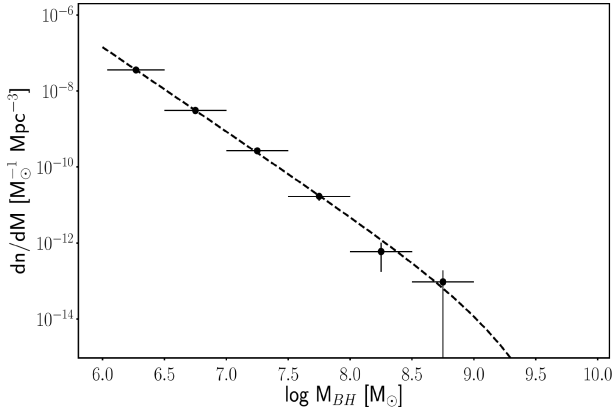


Figure 9. Mass function of wandering black holes ($M_{\text{BH}} \gtrsim 10^6 M_\odot$) computed from the cosmological simulation ROMULUS25 and the best-fitting Schechter function with $M_{\text{BH}}^* = 10^9 M_\odot$ and the best-fitting values of $n_{\text{BH}}^* = 3.11 \times 10^{-5} \text{ Mpc}^{-3}$ and $\alpha = -2.22$.

simulation of higher mass resolution and/or lower black hole seed mass.

The mass density of wandering black holes that follow a Schechter mass function is

$$\rho_{\text{BH}} = \int_{M_{\text{min}}}^{\infty} \frac{dn}{dM_{\text{BH}}} M_{\text{BH}} dM_{\text{BH}} \quad (36)$$

$$= n_{\text{BH}}^* M_{\text{BH}}^* \Gamma(\alpha + 2, M_{\text{min}}/M_{\text{BH}}^*),$$

with $\Gamma(\alpha, x)$ the upper incomplete Gamma function. Here, we have introduced a lower mass limit, M_{min} , in order to avoid singularities for integer values of $\alpha \leq -2$. Throughout we adopt $M_{\text{min}} =$

$10^2 M_\odot$, which roughly corresponds to the mass scale below which perturbing black holes are no longer detectable (see Fig. 5). Similarly, the expectation value for the number of distortions along a given lensing arc is given by

$$\lambda_{\text{dis}} = \int_0^{\infty} V_{\text{eff}}(M_{\text{BH}}) \frac{dn}{dM_{\text{BH}}} dM_{\text{BH}} \quad (37)$$

$$= n_{\text{BH}}^* \int_0^{\infty} V_{\text{eff}}(x M_{\text{BH}}^*) x^\alpha e^{-x} dx,$$

where $V_{\text{eff}}(M_{\text{BH}})$ is given by equation (26). Note that, since $V_{\text{eff}} \rightarrow 0$ for $M_{\text{BH}} \lesssim 10^3 M_\odot$, here we do not need to cut off the mass integral below M_{min} .

Using these expressions, we can transform the confidence interval ($\lambda_{\text{lower}}, \lambda_{\text{upper}}$) corresponding to a given number of detected distortions, N_{dis} , into corresponding constraints on n_{BH}^* and α . In particular, for a null-detection, we have that $\lambda_{\text{dis}} < 1.83$ and 5.30 at 68 and 99 per cent confidence levels, respectively. Using equation (36), these constraints can then be transformed into constraints on $\Omega_{\text{BH}}/\Omega_{\text{DM}}$. Fig. 10 shows such constraints for a null-detection along our fiducial arc when observed with $\mathcal{R} = 0.8$ mas. The shaded regions mark the 68 and 99 per cent confidence regions and indicate that such a null-detection allows one to rule out $n_{\text{BH}}^* \gtrsim 1 \text{ Mpc}^{-3}$ for $\alpha \simeq -2$. For a significantly steeper mass function, that is, smaller values of α , the constraining power with respect to n_{BH}^* rapidly diminishes. The thick, solid lines correspond to constant values of $\Omega_{\text{BH}}/\Omega_{\text{DM}}$ of 1, 0.01, and 0.0001, as indicated.

As is evident, a null-detection along our fiducial curve basically rules out that the majority of dark matter is in the form of black holes characterized by a Schechter-like mass function. The green dot marks the values of α and n_{BH}^* for the mass function of wandering black holes in the ROMULUS25 simulation (cf. Fig. 9). Note

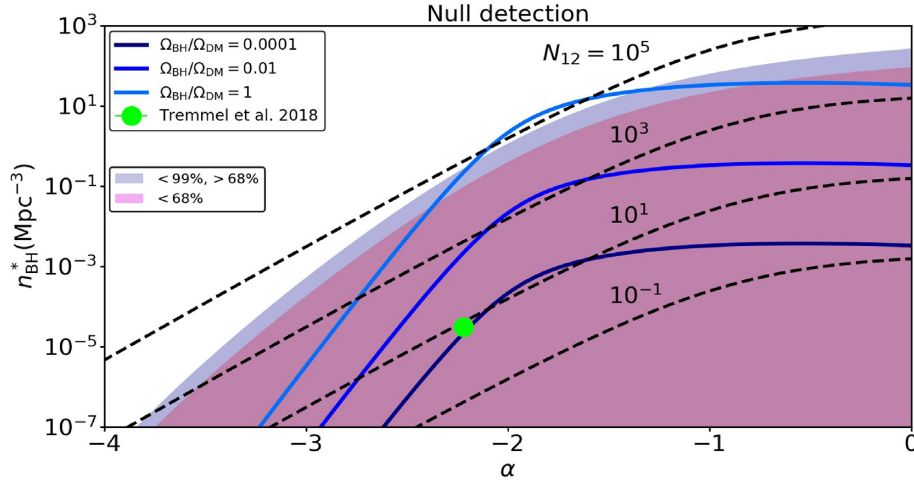


Figure 10. Single null detection: contours of n_{BH}^* versus α for different values of the occupation number N_{12} for wandering black holes (dashed lines) and for different values of $\Omega_{\text{BH}}/\Omega_{\text{DM}}$ (solid lines). The shaded region represents the allowed values of $n_{\text{BH}}^* - \alpha$ for a null detection of lensing distortion events, given the fiducial configuration ($z_S = 2.056$, $z_L = 0.881$, $\mathcal{R} = 0.8$ mas, $M_{L(\theta_E)} = 10^{12} M_\odot$). The two different shades from top to bottom indicate the 99 and 68 percent confidence levels. The green dot represents the values of n_{BH}^* and α obtained by Tremmel et al. (2018b) in their cosmological simulation ROMULUS25.

that this estimate is based on the assumption that all SMBHs in ROMULUS25 not located at a galactic nucleus are detectable as free-floating black holes. However, roughly 40 per cent of them reside within 10 kpc from the central galaxy in the halo in which they orbit. For sufficiently close separations (in projection), it may not be possible, or at least be much harder, to detect the wandering black hole, as the (central) galaxy may dominate the gravitational deflection. We have not attempted to account for this, and therefore caution the reader that the ROMULUS25 prediction shown is likely to be somewhat too optimistic. But even in that case, it is clear that being able to rule-out such a prediction requires data that represents an improvement of several orders of magnitude compared to what is achievable with our single, fiducial arc.

It is useful to translate the above constraints on the number density and power-law slope of the black hole mass function, into constraints on the halo occupation statistics of wandering black holes. Let $\langle N_\bullet \rangle$ denote the number of wandering black holes with mass $M_{\text{BH}} \geq 10^6 M_\odot$ in a halo of mass M_h . Motivated by the occupation statistics of galaxies (see Wechsler & Tinker 2018 for a comprehensive review), we assume that their occupation number scales linearly with halo mass, that is,

$$\langle N_\bullet \rangle(M_h) = N_{12} \left(\frac{M_h}{10^{12} M_\odot} \right), \quad (38)$$

where N_{12} is the *average* number of wandering black holes in a halo of mass $M_h = 10^{12} M_\odot$. If we now assume that the dark matter haloes follow the Sheth & Tormen (2002) halo mass function, $n_h(M_h, z) = dn_h/dM_h$, then the number density of wandering black holes at redshift z is given by

$$n_\bullet(z) = \int_0^\infty \langle N_\bullet \rangle(M_h) n_h(M_h, z) dM_h = \left(\frac{N_{12}}{10^{12} M_\odot} \right) \bar{\rho}_m(z), \quad (39)$$

where we have used that the matter density at redshift z is given by

$$\bar{\rho}_m(z) = \int_0^\infty M_h n_h(M_h, z) dM_h. \quad (40)$$

If we assume that these SMBHs follow the mass function of equation (35), then their number density can also be written as

$$n_{6+} \equiv \int_{10^6}^\infty \frac{dn}{dM_{\text{BH}}} dM_{\text{BH}} = n_{\text{BH}}^* \Gamma(\alpha + 1, 10^{-3}). \quad (41)$$

Equating n_{6+} with $n_\bullet(z = 0)$, we obtain that

$$N_{12} = \left(\frac{10^{12} M_\odot n_{\text{BH}}^*}{\rho_{m,0}} \right) \Gamma(\alpha + 1, 10^{-3}). \quad (42)$$

We can use this expression to translate our constraints on n_{BH}^* and α into constraints on the halo occupation statistics as characterized by N_{12} . The dashed, black contours in Fig. 10 correspond to contours of fixed N_{12} as labelled. If α is in the range $-2.5 < \alpha < -1$, then a null-detection along our fiducial arc implies that $N_{12} < 10^4$ to 10^5 . Again, this is far from the occupation numbers predicted by the ROMULUS25 simulations, which has $N_{12} = 11.2 \pm 8.4$.⁴

Another way to portray these results is to compute, for a given α and n_{BH}^* , the probability that one detects at least one distortion along our fiducial arc. Under our assumption of Poisson statistics, this probability is

$$P(N_{\text{dis}} \geq 1) = 1 - e^{-\lambda_{\text{dis}}}, \quad (43)$$

where λ_{dis} is given by equation (37). Results are presented in Fig. 11, which shows the probability $P(N_{\text{dis}} \geq 1)$ as a function of α . Different curves correspond to different values of n_{BH}^* , as indicated, and the solid dot indicates the halo occupation prediction of Tremmel et al. (2018b). If their prediction is correct, the probability of detecting at least one distortion along our fiducial arc, with a resolution of $\mathcal{R} = 0.8$ mas, is only $\sim 10^{-3}$. Put differently, of order 10^3 , such arcs are required before we may reasonably expect to detect a distortion.

However, as shown in Section 5.1 above, being able to observe at a higher spatial resolution, and finding razor-thin arcs at higher redshifts, may bring this number down considerably. As the number of high-resolution, razor-thin lensing arcs continues to increase, so will our ability to improve on these constraints; it remains to be

⁴Tremmel et al. (2018b) quote an occupation number of 12.2, but that includes the SMBH in the centre of the central galaxy.

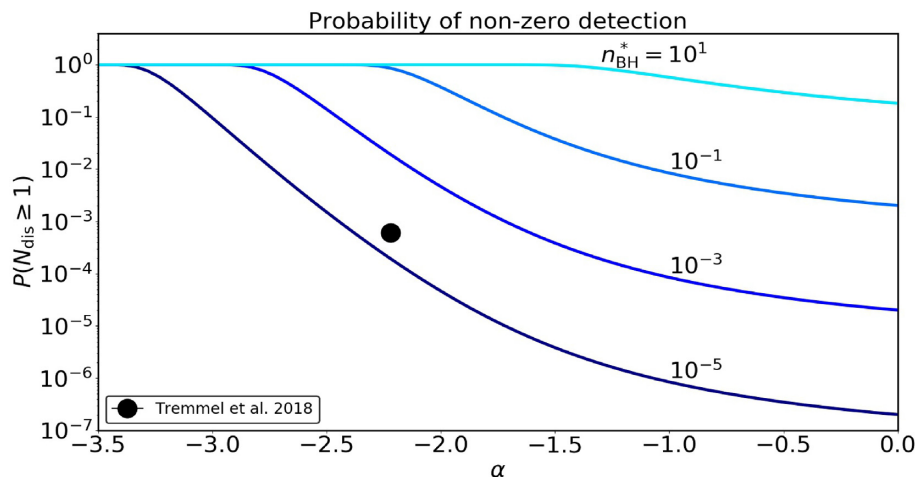


Figure 11. Probability of non-zero detection of wandering black holes of mass ranging from $10^2 M_\odot$ to $10^{10} M_\odot$ from the distortions of a strong gravitational lensing arc of the fiducial lens system as a function of α for different values of n_{BH}^* . The black dot represents the probability of a non-zero detection corresponding to the wandering SMBH occupation number in a Milky Way sized halo and α obtained by Tremmel et al. (2018b) in their cosmological simulation ROMULUS25.

seen whether enough statistics can be accumulated for this test to become meaningful. Future radio surveys with the Square Kilometre Array (SKA) are projected to detect of order 10^5 gravitational lensed active galactic nucleus in the radio (McKean et al. 2015). Such sample sizes, coupled with a VLBI capability for the SKA, would turn the method discussed in this paper into an extremely competitive probe of the mass function of free-floating black holes.

6 CONCLUSION

Razor-thin lensing arcs, with sub-mas width, are ideal probes of the coarseness of the matter distribution along the line of sight towards the source that is being lensed. The thinness of the arcs implies a high sensitivity to detecting lensing distortions due to relatively low-mass objects. In particular, the presence of a free-floating black hole at a sufficiently small impact parameter along the line of sight will cause kink-like distortions in the arc (see Fig. 7) that will be detectable if the black hole is sufficiently massive. Here, free-floating black holes are defined as relatively massive black holes ($M_{\text{BH}} \gtrsim 10^2 M_\odot$) that are sufficiently separated from any galaxy such that they may be considered as isolated for the purpose of computing the lensing distortions on the razor-thin arcs. They basically fall in two categories: PBHs, that form at early times during the radiation dominated era, and wandering black holes that arise as a consequence of the formation and evolution of SMBHs in galactic nuclei.

In this paper, we have investigated the constraints on the number density of free-floating black holes that one may expect to achieve from observations of kink-like distortions of razor-thin arcs, or a lack thereof. Using the double-lens equation, we compute the extent of these kink-like distortions, which we deem detectable ‘by eye’ (i.e. without any complicated lens modelling of the arc surface brightness distribution) as long as the difference in the perturbations along the radial direction, measured at two different positions along the arc, is larger than half the FWHM of the observation. At a resolution of $\mathcal{R} \sim 0.8$ mas, which is relatively straightforward to achieve with current VLBI facilities at cm-wavelengths, the minimum mass of a perturbing black hole that is detectable is roughly $10^3 M_\odot$.

We have computed the constraints on the mass and number density of free-floating black holes that are achievable with a fiducial razor-thin arc of length $\omega_{\text{arc}} \sim 270$ mas and an unresolved width equal to the resolution $\mathcal{R} \sim 0.8$ mas. For our fiducial arc, we assume that the source is located at a redshift $z_s = 2.056$, while the main lens is at $z_L = 0.881$. These values are comparable to those of a razor-thin arc observed from the gravitational lens JVAS B1938+666 with global VLBI at 1.7 GHz (McKean et al. in preparation). If no kink-like distortions are found along such a fiducial arc, one infers that the matter density of free-floating black holes is $\Omega_{\text{BH}} < 0.056 \Omega_{\text{DM}}$ for $M_{\text{BH}} \approx 10^6 M_\odot$. This is similar to the existing constraint from quasar milli-lensing (Wilkinson et al. 2001). The constraints will improve with increasing total arc length (i.e. more arcs), with increasing source redshift, and, above all, with improved resolution, \mathcal{R} . In fact, the constraint on $\Omega_{\text{BH}}/\Omega_{\text{DM}}$ scales with \mathcal{R}^5 for black holes with a mass below the characteristic mass $M_0 \simeq 3 \times 10^4 M_\odot (\mathcal{R}/\text{mas})^2 (D_s/\text{Gpc})$. For black holes with $M_{\text{BH}} \gg M_0$, the constraints have a weak dependence on \mathcal{R} . A null-detection along our fiducial arc, but with a resolution of $\mathcal{R} = 0.2$ mas, which might be achievable in the near future through observations at a higher frequency, would imply $\Omega_{\text{BH}} < 0.013 \Omega_{\text{DM}}$ for $M_{\text{BH}} \approx 10^5 M_\odot$.

To put these constraints in perspective, we have examined the demographics of wandering black holes in the state-of-the-art hydrodynamical simulation ROMULUS25 (Tremmel et al. 2018b), which predicts of order 10 wandering black holes with mass $M_{\text{BH}} > 10^6 M_\odot$ per Milky-Way-like halo. The mass function is well fit by a Schechter function with slope $\alpha \sim -2.2$ and characteristic cut-off mass $M_{\text{BH}}^* \sim 10^9 M_\odot$. If we assume that the occupation number of wandering black holes scales linearly with halo mass, the implied mass density of wandering black holes with mass $M_{\text{BH}} > 10^3 M_\odot$ is of order $\Omega_{\text{BH}} = 10^{-4} \Omega_{\text{DM}}$. This is more than three orders of magnitude lower than the constraints achievable with our fiducial arc. Put differently, if the predictions of ROMULUS25 are correct, and there is no additional contribution from PBHs, then the probability of detecting a kink-like distortion due to a free-floating black hole along our fiducial arc is only $\sim 10^{-3}$.

Hence, we are left to conclude that razor-thin arcs, observed at sub-mas resolution, can only provide competitive constraints on the mass density of free-floating black holes if the astronomical

community is able to amass a large sample of razor-thin arcs, preferentially associated with sources at high redshift, and observed with the highest-possible spatial resolution. On a positive note, it is important to point out that we have only considered kink-like distortions that are detectable ‘by eye’. When using sophisticated image analysis techniques, similar to what has been used for a number of existing lenses at optical and mm-wavelengths (e.g. Vegetti et al. 2010, 2012, 2014; Hezaveh et al. 2016b), we expect that one ought to be able to improve sensitivity by at least an order of magnitude, resulting in a similar order of magnitude improvement in the constraints on $\Omega_{\text{BH}}/\Omega_{\text{DM}}$. Hence, we remain optimistic that razor-thin arcs will prove to be a powerful probe of the coarseness of the matter distribution on cosmological scales, and of the mass density of free-floating black holes in particular.

ACKNOWLEDGEMENTS

We are grateful to Dhruva Dutta Chowdhury, Johannes Lange, Tim Miller, and Nir Mandelker for help and useful discussions, and to the anonymous referee for valuable comments and suggestions. FvdB is supported by the National Aeronautics and Space Administration under grant no. 17-ATP17-0028 issued through the Astrophysics Theory Program and by the US National Science Foundation through grant AST 1516962 and receives additional support from the Klaus Tschira foundation. FvdB, AM, and SM are grateful to the Kavli Institute for Theoretical Astrophysics at University of California Santa Barbara for support that promoted some of the early discussions regarding this research. SM was supported by Japan Society for the Promotion of Science Kakenhi grant no. 16H01089. This work was supported by World Premier International Research Center Initiative (WPI Initiative), MEXT, Japan.

REFERENCES

Afshordi N., McDonald P., Spergel D. N., 2003, *ApJ*, 594, L71
 Ali-Haïmoud Y., Kamionkowski M., 2017, *Phys. Rev. D*, 95, 043534
 ALMA Partnership et al., 2015, *ApJ*, 808, L4
 Bayer D., Chatterjee S., Koopmans L. V. E., Vegetti S., McKean J. P., Treu T., Fassnacht C. D., 2018, preprint ([arXiv:1803.05952](https://arxiv.org/abs/1803.05952))
 Bellovary J. M., Governato F., Quinn T. R., Wadsley J., Shen S., Volonteri M., 2010, *ApJ*, 721, L148
 Birrer S., Amara A., Refregier A., 2017, *J. Cosmol. Astropart. Phys.*, 5, 037
 Brandt T. D., 2016, *ApJ*, 824, L31
 Carr B., Silk J., 2018, *MNRAS*, 478, 3756
 Carr B., Kühnel F., Sandstad M., 2016, *Phys. Rev. D*, 94, 083504
 Carr B. J., Lidsey J. E., 1993, *Phys. Rev. D*, 48, 543
 Chen M. C., Broadhurst T., Lim J., Diego J. M., Ohya Y., Ford H., Benítez N., 2018, *ApJ*, 863, 135
 Dalal N., Kochanek C. S., 2002, *ApJ*, 572, 25
 Deane R. P. et al., 2014, *Nature*, 511, 57
 Despali G., Vegetti S., White S. D. M., Giocoli C., van den Bosch F. C., 2018, *MNRAS*, 475, 5424
 Di Cintio A., Tremmel M., Governato F., Pontzen A., Zavala J., Bastidas Fry A., Brooks A., Vogelsberger M., 2017, *MNRAS*, 469, 2845
 Favata M., Hughes S. A., Holz D. E., 2004, *ApJ*, 607, L5
 Garwood F., 1936, *Biometrika*, 28, 437
 González J. A., Sperhake U., Brüggemann B., Hannam M., Husa S., 2007, *Phys. Rev. Lett.*, 98, 091101
 Häring N., Rix H.-W., 2004, *ApJ*, 604, L89
 Hawking S. W., Moss I. G., Stewart J. M., 1982, *Phys. Rev. D*, 26, 2681
 Hezaveh Y., Dalal N., Holder G., Kisner T., Kuhlen M., Perreault Levasseur L., 2016a, *J. Cosmol. Astropart. Phys.*, 11, 048
 Hezaveh Y. D. et al., 2016b, *ApJ*, 823, 37
 Inoue Y., Kusenkov A., 2017, *J. Cosmol. Astropart. Phys.*, 10, 034

Jedamzik K., 1997, *Phys. Rev. D*, 55, R5871
 Jiang F., van den Bosch F. C., 2016, *MNRAS*, 458, 2848
 Jones E., Oliphant T., Peterson P. et al., 2001, SciPy: Open Source Scientific Tools for Python, Available at: <http://www.scipy.org/>
 Keeton C. R., 2001, preprint ([astro-ph/0102340](https://arxiv.org/abs/astro-ph/0102340))
 Keeton C. R., 2003, *ApJ*, 584, 664
 Keeton C. R., Moustakas L. A., 2009, *ApJ*, 699, 1720
 Kodama H., Sasaki M., Sato K., 1982, *Prog. Theor. Phys.*, 68, 1979
 Koopmans L. V. E., 2005, *MNRAS*, 363, 1136
 Leach S. M., Grivell I. J., Liddle A. R., 2000, *Phys. Rev. D*, 62, 043516
 Li R., Frenk C. S., Cole S., Gao L., Bose S., Hellwing W. A., 2016, *MNRAS*, 460, 363
 Li R., Frenk C. S., Cole S., Wang Q., Gao L., 2017, *MNRAS*, 468, 1426
 Mao S., Schneider P., 1998, *MNRAS*, 295, 587
 Mao S., Jing Y., Ostriker J. P., Weller J., 2004, *ApJ*, 604, L5
 Marconi A., Hunt L. K., 2003, *ApJ*, 589, L21
 McKean J. et al., 2015, Advancing Astrophysics with the Square Kilometre Array (AASKA14). p. 84. <http://adsabs.harvard.edu/abs/2015aska.conf E..84M>
 Metcalf R. B., 2005, *ApJ*, 629, 673
 Mo H., van den Bosch F. C., White S., 2010, Galaxy Formation and Evolution. Cambridge Univ. Press, Cambridge
 Mohammed I., Saha P., Liesenborgs J., 2015, *PASJ*, 67, 21
 More A., McKean J. P., More S., Porcas R. W., Koopmans L. V. E., Garrett M. A., 2009, *MNRAS*, 394, 174
 Navarro J. F., Frenk C. S., White S. D. M., 1997, *ApJ*, 490, 493
 Planck Collaboration XVI, 2014, *A&A*, 571, A16
 Powell M. J. D., 1970, Numerical Methods for Nonlinear Algebraic Equations, Gordon and Breach, Philadelphia.
 Quinn D. P., Smith M. C., 2009, *MNRAS*, 400, 2128
 Ricotti M., Ostriker J. P., Mack K. J., 2008, *ApJ*, 680, 829
 Schneider P., Ehlers J., Falco E. E., 1992, Gravitational Lenses. Springer-Verlag Berlin, Heidelberg
 Sheth R. K., Tormen G., 2002, *MNRAS*, 329, 61
 Spingola C., McKean J. P., Auger M. W., Fassnacht C. D., Koopmans L. V. E., Lagattuta D. J., Vegetti S., 2018, *MNRAS*, 478, 4816
 Tremaine S. et al., 2002, *ApJ*, 574, 740
 Tremmel M., Governato F., Volonteri M., Quinn T. R., 2015, *MNRAS*, 451, 1868
 Tremmel M., Karcher M., Governato F., Volonteri M., Quinn T. R., Pontzen A., Anderson L., Bellovary J., 2017, *MNRAS*, 470, 1121
 Tremmel M., Governato F., Volonteri M., Quinn T. R., Pontzen A., 2018a, *MNRAS*, 475, 4967
 Tremmel M., Governato F., Volonteri M., Pontzen A., Quinn T. R., 2018b, *ApJ*, 857, L22
 Treu T., 2010, *ARA&A*, 48, 87
 Vegetti S., Koopmans L. V. E., 2009, *MNRAS*, 400, 1583
 Vegetti S., Koopmans L. V. E., Bolton A., Treu T., Gavazzi R., 2010, *MNRAS*, 408, 1969
 Vegetti S., Lagattuta D. J., McKean J. P., Auger M. W., Fassnacht C. D., Koopmans L. V. E., 2012, *Nature*, 481, 341
 Vegetti S., Koopmans L. V. E., Auger M. W., Treu T., Bolton A. S., 2014, *MNRAS*, 442, 2017
 Vegetti S., Despali G., Lovell M. R., Enzi W., 2018, *MNRAS*, 481, 3661
 Volonteri M., Perna R., 2005, *MNRAS*, 358, 913
 Volonteri M., Dubois Y., Pichon C., Devriendt J., 2016, *MNRAS*, 460, 2979
 Wechsler R. H., Tinker J. L., 2018, *ARA&A*, 56, 435
 Wilkinson P. N. et al., 2001, *Phys. Rev. Lett.*, 86, 584
 Wong K. C., Ishida T., Tamura Y., Suyu S. H., Oguri M., Matsushita S., 2017, *ApJ*, 843, L35

APPENDIX A: SCALING RELATIONS

The effective volume specified in equation (26) has to be computed numerically, and involves numerically solving the perturbative form of the double lens equation to compute $\Delta\beta_{\text{P,max}}(z)$. In order to provide some insight as to how V_{eff} scales with the mass of the

perturber, M_P , and the resolution limit, \mathcal{R} , it is useful to derive some scaling relations by analytically solving the perturbative lens equation under certain extreme conditions.

The perturbative double lens equation given in equation (12) can be analytically solved in certain simplified cases. We shall compute $\delta\vec{\theta}$ in one such simplified foreground case. At the position along the unperturbed arc closest to the perturber (point 1 in Fig. 2), we have that $\theta_{0x1} = 0$ and $\theta_{0y1} = |\vec{\theta}_0|$. Hence, both the magnification and correction tensor (equations 14 and 15) reduce to diagonal form:

$$\mathbf{M}(\vec{\theta}_0) = \begin{bmatrix} \left(1 - \theta_E/|\vec{\theta}_0|\right)^{-1} & 0 \\ 0 & 1 \end{bmatrix} \quad (\text{A1})$$

and

$$\mathbf{C}(\vec{\theta}_0) = \begin{bmatrix} 1 - \gamma_t \theta_E/|\vec{\theta}_0| & 0 \\ 0 & 1 \end{bmatrix}. \quad (\text{A2})$$

Solving equation (12) in the foreground case using the above simplified forms of \mathbf{M} and \mathbf{C} , and the form for α_{DP} given in equation (19), yields

$$\begin{aligned} \delta\theta_{x1} &= 0, \\ \delta\theta_{y1} &= \frac{\theta_{\text{EP}}^2}{\delta\theta_{y1} + \Delta\beta_P}, \end{aligned} \quad (\text{A3})$$

where $\Delta\beta_P = \theta_{0y1} - \beta_{Py} = |\vec{\theta}_0| - \beta_{Py}$ is the angular impact parameter of the perturber with respect to the unperturbed arc. The solution for $\delta\theta_{y1}$ is similar to the expression for the image angle as a function of the angular impact parameter $\Delta\beta_P$ in absence of the main lens:

$$\delta\theta_{y1} = -\frac{\Delta\beta_P}{2} \pm \sqrt{\left(\frac{\Delta\beta_P}{2}\right)^2 + \theta_{\text{EP}}^2}. \quad (\text{A4})$$

Note that if $\Delta\beta_P = 0$, the perturbation of the arc, $\delta\theta_{y1}$, is equal to θ_{EP} , the Einstein angle of the perturber, as expected. Also, note that the tangential perturbation, $\delta\theta_{x1}$ is zero and the radial perturbation, $\delta\theta_{y1}$, is maximum at this point. The solution for $\delta\vec{\theta}$ at this point for the background case yields similar results.

The computation of $\delta\vec{\theta}$ at some other point on the arc is more involved because the magnification and correction tensors now have non-zero off-diagonal terms. At point 2, located an angle ϕ along the unperturbed arc from point 1 (see Fig. 2), we have that $\theta_{0x2} = |\vec{\theta}_0| \sin(\phi)$, and $\theta_{0y2} = |\vec{\theta}_0| \cos(\phi)$. If ϕ is sufficiently small,⁵ then, to first order, $\theta_{0x2} \approx |\vec{\theta}_0| \phi$ and $\theta_{0y2} \approx |\vec{\theta}_0|$. Under this approximation, \mathbf{M} and \mathbf{C} have off-diagonal terms proportional to ϕ and diagonal terms independent of ϕ . Solving for $\delta\vec{\theta}$ using equation (12) for the foreground case, one can obtain the following form for the radial perturbation $\delta\theta_{r2}$ by applying the rotation matrix as in equation (17)

$$\begin{aligned} \delta\theta_{r2} &\approx \phi \delta\theta_{x2} + \delta\theta_{y2} \\ &\approx \frac{\theta_{\text{EP}}^2}{\left(\delta\theta_{x2} + |\vec{\theta}_0| \phi\right)^2 + \left(\delta\theta_{y2} + \Delta\beta_P\right)^2} \\ &\quad \times \left[|\vec{\theta}_0| \phi^2 + \delta\theta_{r2} + \Delta\beta_P\right], \end{aligned} \quad (\text{A5})$$

where $\Delta\beta_P = \theta_{0y2} - \beta_{Py} \approx |\vec{\theta}_0| - \beta_{Py}$.

Ignoring the perturbations in the equations (A3) and (A5) relative to $\Delta\beta_P$ and $|\vec{\theta}_0| \phi$, we have the following expressions for $\delta\theta_{r1}$ and

$$\delta\theta_{r2}$$

$$\delta\theta_{r1} \approx \frac{\theta_{\text{EP}}^2}{\Delta\beta_P}, \quad (\text{A6})$$

$$\delta\theta_{r2} \approx \frac{\theta_{\text{EP}}^2}{|\vec{\theta}_0|^2 \phi^2 + (\Delta\beta_P)^2} \left[|\vec{\theta}_0| \phi^2 + \Delta\beta_P\right].$$

Implementing the limiting case of the detectability criterion given in equation (22), i.e. $\Delta\theta_r = \delta\theta_{r1} - \delta\theta_{r2} = \mathcal{R}/2$, we obtain the following equation for $\Delta\beta_{P,\text{max}}$

$$(\Delta\beta_{P,\text{max}})^3 + \Delta\beta_{P,\text{max}} \left(|\vec{\theta}_0| + \frac{2\theta_{\text{EP}}^2}{\mathcal{R}} \right) |\vec{\theta}_0| \phi^2 - \frac{2\theta_{\text{EP}}^2}{\mathcal{R}} |\vec{\theta}_0|^2 \phi^2 = 0. \quad (\text{A7})$$

In the background case, $\Delta\beta_{P,\text{max}}$ follows a similar equation, but with $|\vec{\theta}'_0| = |\vec{\theta}_0| - \gamma_b \theta_E$ replacing $|\vec{\theta}_0|$.

It can be seen from equation (A7) that the product of the roots, $(2\theta_{\text{EP}}^2/\mathcal{R}) |\vec{\theta}_0|^2 \phi^2$, is positive definite, whereas the sum of the roots, i.e. the coefficient of the quadratic term, is equal to zero. This implies that the equation has only one positive real root. As we demonstrate below, this root behaves differently for small and large z_P .

We can also derive an approximate expression for $M_{P,\text{min}}$, the minimum BH mass that can be detected at a given redshift. The maximum distortion is caused when the impact parameter is equal to zero, in which case the radius of the kink-like distortion, $\delta\theta_{y1}$, at point 1 (see Fig. 2), is equal to the Einstein radius of the perturbing black hole. Hence, based on our detectability criterion (equation 22), $M_{P,\text{min}}$ corresponds to the mass for which $\theta_{\text{EP}} = \mathcal{R}/2$. This translates to

$$M_{P,\text{min}}(z_P) = \frac{\mathcal{R}^2 c^2}{16G} \frac{D_P D_S}{D_{PS}} \equiv M_0 \frac{D_P}{D_{PS}}, \quad (\text{A8})$$

where we have defined the characteristic mass scale

$$M_0 \equiv \frac{\mathcal{R}^2 c^2}{16G} D_S. \quad (\text{A9})$$

For our fiducial case, which has $z_S = 2.056$ and $\mathcal{R} = 0.8$ mas, we have that $M_0 \approx 3.5 \times 10^4 M_\odot$.

In what follows, we use equations (A7) and (A8) to derive approximate expressions for the effective volume, V_{eff} , given by equation (26) in the limits of low mass ($M_P \ll M_0$) and high mass ($M_P \gg M_0$).

A1 Low mass limit

In the low mass limit, i.e. $M_P \ll M_0$, the maximum redshift out to which the perturber can be detected, $z_{P,\text{max}}$ is small, and the effective comoving volume, V_{eff} , comprises only of the foreground volume. In addition, we have that $D_a(z_{P,\text{max}}) \approx r(z_{P,\text{max}}) \approx (c/H_0)z_{P,\text{max}}$. The comoving volume element is given by

$$\frac{d^2 V}{d\Omega dz} = D_H \frac{r^2(z)}{E(z)} \quad (\text{A10})$$

with $D_H = c/H_0$, $r(z)$ the comoving distance out to redshift z , and $E(z) = H(z)/H_0$. At small z , we have that $E(z) \sim 1$, and the expression for the effective comoving volume (equation 26) reduces to

$$V_{\text{eff}} \approx 2 \omega_{\text{arc}} D_H^3 \int_0^{z_{P,\text{max}}} \Delta\beta_{P,\text{max}}(z) z^2 dz. \quad (\text{A11})$$

The maximum redshift, $z_{P,\text{max}}$, is the redshift at which the perturber has an Einstein radius $\theta_{\text{EP}} = \mathcal{R}/2$, and thus where $M_P =$

⁵This is typically the case if the arc length, ω_{arc} , is only a fraction of the entire length of the Einstein ring, $2\pi|\vec{\theta}_0|$.

$M_{P,\min}$. For sufficiently small M_P , this allows us to write

$$z_{P,\max} \approx \frac{M_P}{M_0} \frac{D_S}{D_H}. \quad (\text{A12})$$

For $z_P \ll z_{P,\max}$, $(\Delta\beta_{P,\max})^3$ is the dominant term in equation (A7) and therefore in this limit, $\Delta\beta_{P,\max} \approx \left[\left(2\theta_{EP}^2 |\vec{\theta}_0|^2 \phi^2 \right) / \mathcal{R} \right]^{\frac{1}{3}}$. But for most of the redshift range the second term dominates the first in equation (A7), and

$$\Delta\beta_{P,\max} \approx \left(\frac{2\theta_{EP}^2}{\mathcal{R}} |\vec{\theta}_0| \right) / \left(|\vec{\theta}_0| + \frac{2\theta_{EP}^2}{\mathcal{R}} \right) \approx \frac{2\theta_{EP}^2}{\mathcal{R}}, \quad (\text{A13})$$

where the second approximation follows from the fact that in the small mass limit $|\theta_0| \gg (2\theta_{EP}^2)/\mathcal{R}$. Substituting this value for $\Delta\beta_{P,\max}$ in equation (A11), we finally obtain that

$$V_{\text{eff}}(M_P \ll M_0) \approx 256 \omega_{\text{arc}} \frac{R_s^3}{\mathcal{R}^5}. \quad (\text{A14})$$

Therefore, in the low mass limit, the effective volume scales as

$$V_{\text{eff}}(M_P \ll M_0) \sim \omega_{\text{arc}} \frac{M_P^3}{\mathcal{R}^5}. \quad (\text{A15})$$

A2 Large mass limit

Next, we consider the large mass limit, where $M_P \gg M_0$. Note, though, that we demand that M_P remains small compared to the mass of the main lens, M_L . When M_P is large, we have that $z_{P,\max} = z_S$ and the effective comoving volume therefore comprises of both the foreground and background volumes:

$$V_{\text{eff}} = 2 \omega_{\text{arc}} \int_0^{z_S} \Delta\beta_{P,\max}(z) \frac{r^2(z)}{E(z)} dz. \quad (\text{A16})$$

In this limit, for most of the redshift range, $(\Delta\beta_{P,\max})^3$ is the dominant term in equation (A7), implying that

$$\Delta\beta_{P,\max} \approx \begin{cases} \left[\frac{2\theta_{EP}^2}{\mathcal{R}} |\vec{\theta}_0|^2 \phi^2 \right]^{1/3}, & \text{foreground,} \\ \left[\frac{2\theta_{EP}^2}{\mathcal{R}} |\vec{\theta}'_0|^2 \phi^2 \right]^{1/3}, & \text{background,} \end{cases} \quad (\text{A17})$$

where $|\vec{\theta}'_0| = |\vec{\theta}_0| - \gamma_b \theta_E$. Substituting in equation (A16), and using that $\phi = (f \omega_{\text{arc}})/(2|\theta_0|)$, we finally obtain that in the large mass limit the effective volume scales as

$$V_{\text{eff}}(M_P \gg M_0) \sim (\omega_{\text{arc}})^{\frac{5}{3}} f^{\frac{2}{3}} \left(\frac{M_P}{\mathcal{R}} \right)^{\frac{1}{3}}. \quad (\text{A18})$$

From the two different scaling dependences of V_{eff} in the two limits, one can define a turnover mass M_{TO} by equating the expressions for V_{eff} in the low and high mass limits. This yields

$$M_{\text{TO}} \approx 4 \times 10^5 \left(\frac{f}{0.5} \right)^{\frac{1}{4}} \left(\frac{\omega_{\text{arc}}}{270 \text{ mas}} \right)^{\frac{1}{4}} \left(\frac{\mathcal{R}}{0.8 \text{ mas}} \right)^{\frac{7}{4}} \times \left(\frac{r(z_S)}{1 \text{ Gpc}} \right)^{\frac{5}{8}} M_{\odot}, \quad (\text{A19})$$

which is about an order of magnitude larger than the characteristic mass M_0 . Note that M_{TO} characterizes the mass at which the mass-

scaling of the effective volume changes its behaviour, and roughly corresponds to the mass at which the constraints on $\Omega_{\text{BH}}/\Omega_{\text{DM}}$ are most strict (cf. Fig. 8).

APPENDIX B: DISTORTIONS DUE TO NFW HALOES

In this paper, we examine how *localized* kink-like distortions of gravitational arcs can be used to constrain the number density of free-floating black holes. However, one might envision other objects to cause similar distortions. In particular, in the Λ CDM paradigm one expects a large abundance of dark matter haloes spanning many orders of magnitude in halo mass. These haloes are predicted to have a universal Navarro-Frenk-White (NFW) density profile (Navarro, Frenk & White 1997), and each halo in turn is predicted to have a hierarchy of substructures (e.g. Jiang & van den Bosch 2016). One might worry that such dark matter (sub)haloes along the line of sight cause similar distortions of razor-thin lensing arcs, and thereby ‘confuse’ our interpretation in terms of free-floating black holes. After all, several groups are using distortions of gravitational lenses to probe dark matter (sub)-structure (e.g. Koopmans 2005; More et al. 2009; Vegetti & Koopmans 2009; Vegetti et al. 2010, 2012; Hezaveh et al. 2016b; Birrer et al. 2017). However, because of their wildly different density profiles, the lensing distortions caused by black holes cannot be confused for distortions caused by NFW haloes.

To illustrate this, Fig. B1 compares the distortions due to a black hole of mass $M_P = 10^7 M_{\odot}$ (upper panel) to those due to an NFW halo of mass $M_{\text{vir}} = 10^{10} M_{\odot}$ and with a concentration parameter $c_{\text{vir}} = 10$ (lower panel). These have been computed by numerically solving the perturbative form of the double lens equation (12). In each case, we show the results for three different angular impact parameters, and we also indicate the value of $2\Delta\theta_t/\mathcal{R}$; this ratio needs to be larger than unity for the perturbation to be considered ‘detectable’ according to our criterion (equation 22). In the case of the black hole, the perturbations easily satisfy our detection criterion, for all three values of the angular impact parameter. In the case of the NFW halo, though, $2\Delta\theta_t/\mathcal{R} < 0.1$ for all cases shown, and these distortions are therefore not ‘detectable’ based on our criterion. The reason is that the distortions are not sufficiently localized. Rather, the arc is merely displaced from its unperturbed location. An NFW perturber causes a maximal displacement of the arc when the impact parameter with respect to the unperturbed arc is approximately equal to the halo’s scale radius. For the halo considered here, the scale radius is $r_s \approx 7.5 \text{ kpc}$, which corresponds to an angular impact parameter of $\approx 3.5 \times 10^4 \text{ mas}$ at the redshift of the perturber (here taken to be $z_P = 0.01$). Note that the NFW perturber has a mass that is 1000 times larger than that of the black hole; if we were to consider an NFW perturber with a mass of $10^7 M_{\odot}$, the ‘displacement’ of the arc would be a factor of 100 smaller, and the maximum value of $2\Delta\theta_t/\mathcal{R}$ would be only ~ 0.008 . Hence, under no circumstance can NFW haloes along the line of sight cause localized, kink-like distortions such as those due to black hole perturbers.

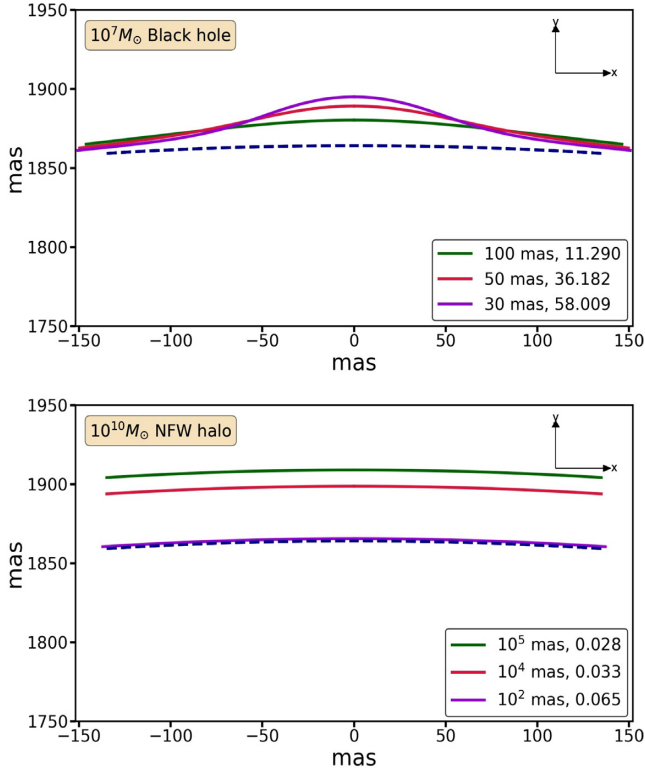


Figure B1. The upper panel shows the perturbed arcs due to a $10^7 M_{\odot}$ black hole at $z_p = 0.01$ for three different values of the angular impact parameter $\Delta\beta_p$. Here, we consider our fiducial lensing configuration with $z_L = 0.881$, $z_S = 2.056$, $M_L(\theta_E) = 10^{12} M_{\odot}$, and $|\beta_S| = 36$ mas. The lower panel shows the perturbed arcs in the presence of an NFW halo perturber with $M_{\text{vir}} = 10^{10} M_{\odot}$ and $c_{\text{vir}} = 10$. The corresponding values of $2\Delta\theta_r/\mathcal{R}$ (assuming the fiducial value of $\mathcal{R} = 0.8$ mas and $f = 0.5$) are also indicated. If this ratio is larger than unity, the perturbation is deemed detectable according to our criterion (equation 22). As is evident, whereas the black hole perturber is detectable for all three impact parameters shown, the distortions due to the NFW halo are not sufficiently localized to pass our detection criterion.

This paper has been typeset from a \LaTeX file prepared by the author.